L-Alanine Dehydrogenase from *Vagococcus lutrae*: Structural Analysis and Industrial Potential

by

Cengiz Kaan Ferah

A Dissertation Submitted to the
Graduate School of Sciences and Engineering
in Partial Fulfillment of the Requirements for
the Degree of

Master of Science

in

Molecular Biology and Genetics

KOÇ ÜNİVERSİTESİ

May 22, 2025

L-Alanine Dehydrogenase from *Vagococcus lutrae*: Structural Analysis and Industrial Potential

Koç University

Graduate School of Sciences and Engineering

This is to certify that I have examined this copy of a master's thesis by

Cengiz Kaan Ferah

and have found that it is complete and satisfactory in all respects,
and that any and all revisions required by the final
examining committee have been made.

Committee Members:

_____

Assist. Prof. Hasan Demirci

_____

Assist. Prof. Onur Öztaş

_____

Assoc. Prof. Özge Şensoy

Date: _____

To my dear family...

ABSTRACT

L-Alanine Dehydrogenase from *Vagococcus lutrae*: Structural Analysis and Industrial Potential

Cengiz Kaan Ferah

Master of Science in Molecular Biology and Genetics

May 22, 2025

L-Alanine dehydrogenase from *Vagococcus lutrae* (*Vl*AlaDH) catalyzes the reversible oxidation-reduction reaction between L-alanine and pyruvate. The enzyme's ability to generate a valuable product in a single enzymatic step has increased interest in bacterial AlaDHs. In this study, a novel wild-type apo structure of AlaDH from under characterized organism is presented which could serve as a candidate for L-alanine production with minimal pyruvate byproduct. The discovery lays the groundwork for future studies for protein engineering has been laid.

The structure was determined using highly complex experimental methodology of X-ray crystallography with the "*Turkish Delight*" diffractometer in the ambient temperature in near neutral pH. This approach enabled the determination of the apo-structure of *Vl*AlaDH at 3.2 Å resolution revealing a homo-hexamer oligomerization with conserved Rossmann fold motifs.

The main takeaway from the study was the enzyme retained the key motif architecture observed in each homolog structure. The retained motifs being one NAD^+ -binding Rossmann fold connected with conserved α-helices linker to a second Rossmann fold which carried the catalytic residues for pyruvate and L-alanine. Notable differences were observed in the NAD^+-binding Rossmann fold where it carried some similarities in residue level to a thermostable bacterial AlaDHs called *Geobacillus kaustophilus* and *Thermus thermophilus*. Specifically, residue 270 substituted from Asp to Gln, residue 240 also showed change from Val to Ile between *Geobacillus kaustophilus*, and between *Thermus thermophilus* and *Vagococcus lutrae* both carrying Ile at the residue number 198 but not the homologs. These residues participate in NAD^+ binding into the cleft through hydrogen bonds and hydrophobic interactions. As the primary binding substrate being NAD^+, these substitutions may be targeted for future studies. The phylogenetic tree further supports that even the evolutionary distance of the species shared common adaptations at cofactor

level.

Although the current study went in detail structurally how this novel AlaDH compares to the currently available homologs structures in terms of the main substrate and the cofactors might bind, without experimental validation with crystallizing the protein with the main substrate or cofactor these results stay hypothetical. Additionally, no site-directed mutagenesis trials were performed in order to compare the L-alanine overproduction.

To conclude, the structural, sequential, evolutionary and computational comparison of the L-alanine dehydrogenase from *Vagococcus lutrae* provides valuable insights into substrate and cofactor binding behavior. Information provided in this study even without any co-crystallization or mutagenesis studies, highlights the potential of *Vl*AlaDH for future protein engineering. These findings also support the industrial potential for overproduction of L-alanine biosynthesis and lay a foundation for further optimization efforts.

ÖZETÇE

Vagococcus lutrae kaynaklı L-Alanine dehydrogenase: Yapısal analizi ve Endüstriyel Potensiyeli

Cengiz Kaan Ferah

Moleküler Biyoloji ve Genetik, Yüksek Lisans

1 Ocak 2019

Vagococcus lutrae kaynaklı L-Alanin dehidrogenaz (VlAlaDH), L-alanin ve pirüvat arasındaki geri dönüşümlü oksidasyon-redüksiyon reaksiyonunu katalizler. Enzimin tek bir enzimatik adımda değerli bir ürün üretebilme yeteneği, bakteriyel AlaDH'lere olan ilgiyi artırmıştır. Bu çalışmada, karakterizasyonu sınırlı bir organizmadan elde edilen, yeni bir yabani tip AlaDH apo yapısı sunulmuştur. Bu yapı, minimal pirüvat yan ürünüyle L-alanin üretimi için bir aday olabilir. Bu keşif, gelecekteki protein mühendisliği çalışmaları için bir temel oluşturmaktadır.

Yapı, "Turkish Delight" difraktometresi kullanılarak oda sıcaklığında ve nötr pH'a yakın koşullarda X-ışını kristalografisi yöntemiyle belirlenmiştir. Bu yaklaşım, VlAlaDH'nin 3.2 Å çözünürlüklü apo yapısının belirlenmesini sağlamış ve korunan Rossmann katlanma motiflerine sahip homojen altımerik bir oligomerizasyon ortaya koymuştur.

Çalışmanın temel bulgusu, enzimin her bir homoloğunda gözlemlenen ana motif mimarisini koruduğudur. Korunan motifler, NAD bağlayan bir Rossmann katlanmasını, korunan -sarmallar ile bağlanmış ikinci bir Rossmann katlanmasına bağlayan bir yapıda bulunmuştur; bu ikinci katlanma alanı pirüvat ve L-alanin için katalitik amino asitleri içermektedir. NAD bağlayıcı Rossmann katlanmasında, *Geobacillus kaustophilus* ve *Thermus thermophilus* gibi termostabil bakteriyel AlaDH'lerle amino asit düzeyinde bazı benzerlikler gözlemlenmiştir. Özellikle, 270. pozisyondaki amino asit Asp'dan Gln'a değişmiş, 240. pozisyondaki amino asit Val'den Ile'ye dönüşmüş ve hem *T. thermophilus* hem de *V. lutrae*'de 198. pozisyonda diğer homologlarda bulunmayan bir İzolösin gözlemlenmiştir. Bu amino asitler, NAD'ın bağlanma yarığına hidrojen bağları ve hidrofobik etkileşimler yoluyla katılmaktadır. Ana bağlayıcı kofaktör NAD olduğundan, bu değişimler gelecekteki mühendislik çalışmaları için hedeflenebilir. Filogenetik analiz, evrimsel olarak uzak türlerin kofaktör bağlanması düzeyinde ortak adaptasyonlar gösterdiğini desteklemektedir.

Bu çalışma, bu yeni AlaDH yapısının homolog yapılarla karşılaştırmalı analizini de-

taylı şekilde sunsa da, substrat veya kofaktörle birlikte kristalizasyon yapılmadığı için elde edilen sonuçlar deneysel olarak doğrulanamamaktadır. Ayrıca, L-alanin aşırı üretimiyle karşılaştırılabilecek herhangi bir hedefe yönelik mutagenez çalışması da gerçekleştirilmemiştir.

Sonuç olarak, *Vagococcus lutrae*'ye ait L-alanin dehidrogenazın yapısal, dizisel, evrimsel ve hesaplamalı analizleri, substrat ve kofaktör bağlanma özellikleri hakkında önemli bilgiler sunmaktadır. Kristalleştirme veya mutagenez çalışmaları olmaksızın bile, bu çalışma VlAlaDH'nin gelecekteki protein mühendisliği çalışmaları için umut vadeden bir aday olduğunu göstermektedir. Bulgular ayrıca, L-alanin biyosentezinin endüstriyel üretimi açısından enzimin potansiyelini desteklemekte ve ileri optimizasyon çalışmaları için temel oluşturmaktadır.

ACKNOWLEDGMENTS

I would like to whole hardheartedly thank my advisor Assist. Prof. Hasan Demirci for his unparalleled assitance and guidance in my scientific journey. By being exemplarily role model as a scientist and as a person, pushed me to become better. I would like to pass my gratitude towards other members of my thesis committee, Assist. Prof. Onur Öztaş and Assoc. Prof. Özge Şensoy for taking their valuable time to evaluate my thesis. I also want to thank each member that has been with me through my journey with their friendship, professionalism and drive for being better. Additionally, I would like to thank Prof. Dr. Önder Metin and Prof. Dr. Barış Binay for their help during my research endeavors. My family, the people that were there from the start, I want to thank my mother Emriye, my father Kaan and my little sister Şebnem. This thesis would not be at this form without the never-ending support and belief in my family.

TABLE OF CONTENTS

LIST OF TABLES

LIST OF FIGURES

ABBREVIATIONS

AADH	Amino Acid Dehydrogenase
Ala	Alanine
Ala1(A)	Alanine in the chain 1 A
AlaDH	L-Alanine dehydrogenase
CB-Dock2	Cavity-based protein–ligand docking server version 2
GluDH	Glutamate dehydrogenase
KanR	Kanamycin resistance gene
Kb21(A)	α-ketobutyrate in the chain 1(A)
Kcp1(A)	α-ketocaproate in the chain 1(A)
LDH	Lactate dehydrogenase
LeuDH	Leucine Dehydrogenase
MES	2-(N-morpholino)ethanesulfonic acid
MPC	Mitochondrial pyruvate carrier
MR	Molecular replacement
MSA	Multiple Sequence Alignment
MTZ	Crystallographic reflection data file format
MtAlaDH	*Mycobacterium tuberculosis* L-Alanine dehydrogenase
NAD+	Nicotinamide adenine dinucleotide (oxidized form)
NADH	Nicotinamide adenine dinucleotide (reduced form)
NADPH	Nicotinamide adenine dinucleotide phosphate (reduced form)
NCD	nicotinamide cytosine dinucleotide
Ni-NTA	Nickel–nitrilotriacetic acid
OD600	Optical density at absorbance of 600 nm
PDB	Protein Data Bank
PEG	Poly-ethylene glycol

PISA	Protein Interfaces, Surfaces and Assemblies
PTM	Predicted TM-score
PheDH	Phenylalanine dehydrogenase
PlAlaDH	*Phormidium lapideum* L-Alanine Dehydrogenase
Pyr	Pyruvate
Pyr1(A)	Pyruvate in the chain 1 A
RMSD	Root mean squared deviation
SDF	Structure Data File
SDS	Sodium Dodecyl Sulfate
SDS-Page	Sodium Dodecyl Sulfate–Polyacrylamide Gel Electrophoresis
TCA	Tricarboxylic Acid (Cycle)
Vcell	Unit cell volume
VlAlaDH	*Vagococcus lutrae* L-alanine dehydrogenase
Vm	Matthews coefficient
ald	L-Alanine dehydrogenase gene
pET28(a)+	Expression vector with T7 promoter
pLDDT	Predicted Local Distance Difference Test
˚C	Temperature degree in Celsius
˚K	Temperature degree in Kelvin
ΔG_{diss}	Gibbs Free Energy of Dissociation
ΔG_{int}	Gibbs Free Energy of Interaction
µL	Microliter

Chapter 1

INTRODUCTION

1.1 L-Alanine

L-alanine is an important chemical compound that plays crucial roles in the metabolism of both microorganisms and mammals. The first production of the amino acid was done by German chemist Adolph Strecker by the synthesis method of following a chemical process starting with acetaldehyde. This was decades before it was isolated from biological sources (American Chemical Society, 2021). Acting as a key for nitrogen reservoir, l-alanine participates through transamination and deamination, regulates nitrogen flow and connects the flow to central carbon metabolism (Ohshima & Soda, 1990).

In *Bacillus cereus* and *Bacillus subtilis* species, the central role of L-alanine is carried out by initiation of spore germination. Its function is not only limited to a metabolic substrate but also a signaling molecule. The signaling pathway begins with stereospecific receptors found on dormant cells, binds to L-alanine thus triggering germination. During the early stages of outgrowth, L-alanine is taken up by the cell where it is metabolized into pyruvate and ammonium which serve as necessary supply for energy and biosynthetic precursors (O'Connor & Halvorson, 1961; Siranosian et al., 1993).

In mammals l-alanine plays a key role as a component of glucose-alanine cycle. The process begins with the breakdown of glucose in the muscle cells and formation of pyruvate. Pyruvate then later turned into L-alanine using glutamate via a transaminase enzyme. L-alanine followed by its formation transferred to the liver through bloodstream. Here it transformed into pyruvate to continue with gluconeogenesis pathway. The pathway as described plays a major role in nitrogen transport and energy production for fasting alongside physical exercise (Lennarz & Lane, 2021).

1.2 Pyruvate

Pyruvate is a central three-carbon intermediate connecting multiple essential metabolic pathways. It is produced primarily through glycolysis, where it is one of the products. Pyruvate is also an acting substrate for a wide range of metabolite conversion including acetyl-CoA, lactate, oxaloacetate, and L-alanine, depending on the cell's energy and redox status (Figure 1.1) (Gray et al., 2014; Zangari et al., 2020). Regulating both carbon and nitrogen metabolism by the critical role of pyruvate is carried out with its integration into tricarboxylic acid (TCA) cycle and its reversible conversion with L-alanine via transamination (Ohshima & Soda, 1990; Zangari et al., 2020). In microbial

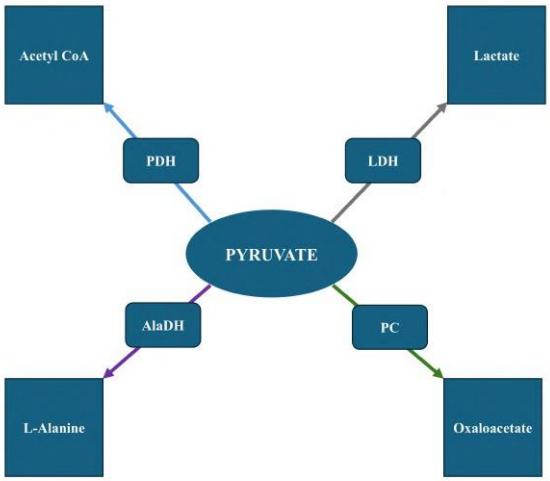

Figure 1.1: Pyruvate as a central metabolic node in bacteria. LDH stands for Lactate dehydrogenase, PDH for Pyruvate dehydrogenase, AlaDH for L-Alanine dehydrogenase and PC for Pyruvate carboxylase. Different pathways colored in different color.

systems, distinct from eukaryotic energy metabolism, pyruvate serves a critical purpose as a metabolic node. It acts as precursor to various fermentation products, aimed to increase the yields of biochemicals, pyruvate is selected as a target in metabolic engineering strategies (Yuan et al., 2022). Furthermore, the mitochondrial pyruvate carrier (MPC) facilitates the import of pyruvate to the mitochondria essentially connecting glycolysis in the cytosol to oxidative phosphorylation inside the mitochondria. Effectively highlighting its importance in cellular energy production (Zangari et al., 2020).

1.3 Industrial Importance of L-Alanine

L-alanine had significant increases in attention as a versatile molecule which touches multiple industries such as food and pharmaceuticals. Altogether making it forefront in industrial biotechnology. The wide usage of L-alanine in industrial settings, describes its potential as flavor enhancer, buffering agent, intermediate in the production of peptides, drugs and biodegradable plastics (Ohshima & Soda, 1990; Hols et al., 1999). L-alanine with its mild sweet taste and metabolic compatibility, is one of the ingredients in parental nutrition formulations and used in oral rehydration (Hols et al., 1999; Vadas & Whitehead, 2008).

Arising from generally harsh reaction conditions of traditional chemical synthesis of L-alanine often results in racemic mixtures. These racemic mixtures in turn, have led the way for the emergence of biotechnological production methods while increasing the sustainability and stereoselectivity of alternatives (Ohshima & Soda, 1990; Vadas & Whitehead, 2008; Yuan et al., 2022).

New advancements in the field of metabolic engineering led to the optimization for high-yield L-alanine production in environments with limited or lack of oxygen in the species of *Corynebacterium glutamicum*, *Lactococcus lactis*, and genus of *Arthrobacter*. The first aspect of the design rationale behind the engineered strains is minimal formation of byproducts by increasing the efficiency of glycolytic flux. Second aspect is diversion of the intermediates toward the reaction side of L-Alanine biosynthesis (Figure 1.2) (Padrosa et al., 2021; Hols et al., 1999; Galkin et al., 1999). Additionally, the use of the redox-balance platforms of fermentation for L-alanine production makes way of cofactor recycling and energy efficient synthesis. All of it reinforces its potential as a green alternative in biotechnology (Kobayashi et al., 2014).

1.4 Industrial Importance of Pyruvate

Pyruvate with its critical roles in industrial biotechnology due to its plentiful roles as precursor, building block, and functional additive in valuable commercial sectors. The commercial sector that makes use of these molecules spans across pharmaceuticals, nutraceuticals, cosmetics, and chemical synthesis, with its sodium salt commonly used in cell

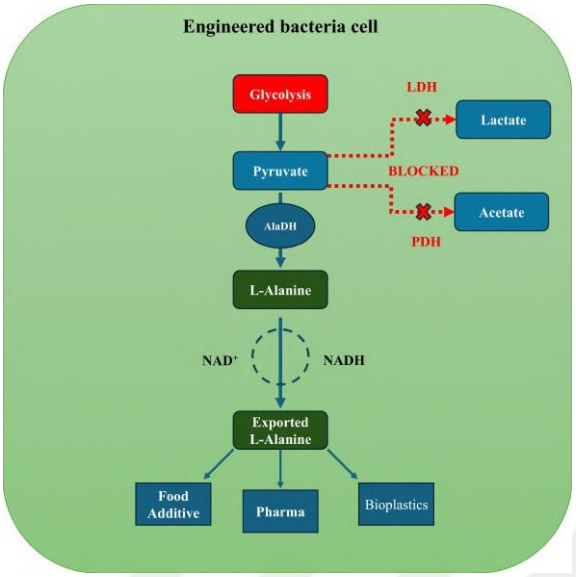

Figure 1.2: Engineered L-alanine over production pathway in engineered bacterial fermentation systems. LDH stands for Lactate dehydrogenase and PDH stands for Pyruvate dehydrogenase. The produced L-Alanine further uses shown below

culture media and medical formulations due to its antioxidative and protective properties (Gray et al., 2014; Xu et al., 2008; Zangari et al., 2020).

In addition to its direct use as a compound, pyruvate can be served as the metabolic precursor to the several value-added compounds such as L-alanine, acetoin, L-valine and organic acids. This highlights its industrial relevance (Xu et al., 2008; Yuan et al., 2022).

The growing demand for stereochemically pure and sustainable pyruvate production has shifted towards the focus into biotechnology, microbial fermentation in particular, to be an environmentally friendly alternative to chemical synthesis. Traditional synthesis processes often carry out complex processing steps, toxic reagents, and high energy input (Yuan et al., 2022).

On the contrary, a more sustainable approach is offered by microbial fermentation. Namely engineered strains *Escherichia coli*, *Corynebacterium glutamicum*, *Torulopsis glabrata*, and *Bacillus subtilis*, with reference to qualities of aerobic and oxygen-limited conditions have been optimized to accumulate high levels of pyruvate (Yuan et al., 2022; Xu et al., 2008). Included modifications are suppression of competing metabolic branches, enchantment of glycolytic flux, and tuning of redux balance to favor pyruvate accumulation.

Improved yields were achieved by process optimizations, such as fed-batch fermentation and repeated batch cultures (Gerharz et al., 2005). This accumulation process has been enhanced with efficiency and scalability in some systems have been increased by the downstream recovery of pyruvate by using membrane-based purification or electrodialysis (Gerharz et al., 2005).

1.5 NAD^+ (Nicotinamide Adenine Dinucleotide)

Nicotinamide adenine dinucleotide (NAD^+) is found to be an essential coenzyme among all the living organisms. The primary function of it is the molecules for electron acceptors in oxidation-reduction reaction mechanisms, also found in numerous other enzymatic reactions. By oxidizing of the molecule NAD^+ is reduced to NADH by receiving electron. The reduced form promotes energy production via processes including glycolysis, the tricarboxylic acid (TCA) cycle, and oxidative phosphorylation (Lennarz & Lane, 2021).

NAD^+ serves as the primary cofactor in the oxidative deamination of amino acids, L-Alanine dehydrogenase (AlaDH) can be given as example. AlaDH catalyzes the conversion of L-alanine to pyruvate, transfer of electrons happens to NAD^+ which then reduced to NADH during the catalysis reaction. Carbon and nitrogen metabolism connection on the molecular level makes the process of generation of NAD^+ easier, making it an essential component for both energy production and biosynthesis (Ohshima & Soda, 1990).

Next to its catalytic role, the level and abundance of the cofactor affect metabolic pathways. It can be factored in the alteration of biosynthetic activities. Enzymes such as AlaDH effective binding and recycling the NAD^+ can have direct influence on l-alanine turnover and product yield (Ohshima & Soda, 1990). Variations in NAD^+ affinity or intracellular NAD^+/NADH ratios may therefore modify enzymatic efficiency, influencing overall metabolic flow in both physiological and industrial settings (Gray et al., 2014; Yuan et al., 2022).

1.6 L-Alanine Dehydrogenase

L-alanine dehydrogenase (AlaDH; EC 1.4.1) causes L-alanine to be reversibly oxidized to pyruvate simultaneously reducing NAD^+ to NADH (Figure 1.4). Especially in nutrient-

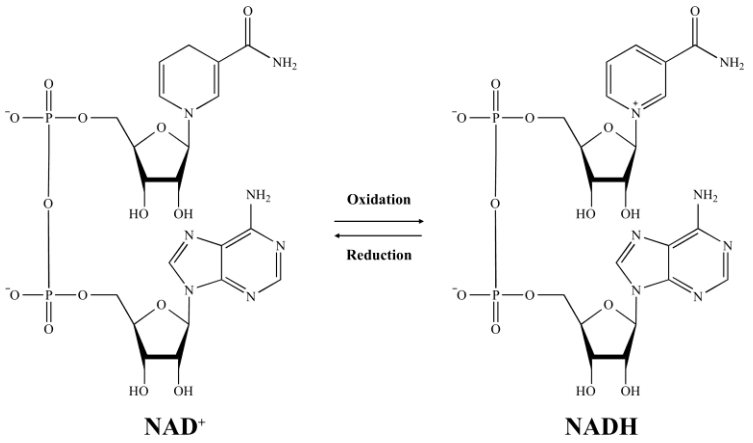

Figure 1.3: NAD^+ to NADH conversation reaction via oxidation and reduction

deficient or demanding environments, microbial nitrogen and carbon metabolism depend on this process entirely. Some identified AlaDH expressing microorganisms can be listed as *Bacillus subtilis*, *Streptomyces spp.*, *Anabaena cylindrica*, *Thermus thermophilus*, *Arthrobacter* species, and psychophilic bacteria including *Colwellia* and *Marinomonas* (Ohshima & Soda, 1979; Itoh & Morikawa, 1985; Galkin et al., 1999; Kobayashi et al., 2014; Wakayama et al., 2008).

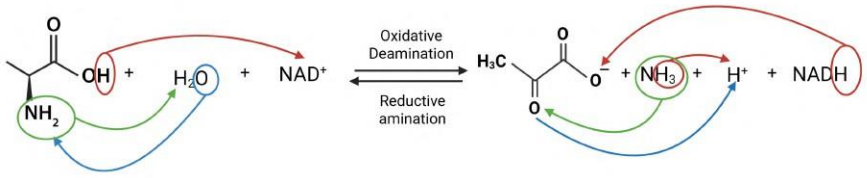

Figure 1.4: L-Alanine dehydrogenase main mechanism showing reversible reaction of pyruvate to L-Alanine. The molecular transfers are shown with differently colored arrows

Unlike certain other dehydrogenases such as formate dehydrogenase, which are able to function with a range of cofactors and coenzymes. This fact is not valid for AlaDH since it is only NAD^+ dependent (Maia et al., 2017).

The Rossmann fold (Figure 1.5) domain binds NAD^+ via conserved GxGxxG motifs and other hydrogen bonding networks, therefore providing structural basis for this selec-

tivity (Lesk, 1995; Ohshima & Soda, 1990). Overall oligomeric organization is mostly hexameric, each AlaDH enzymes have molecular weights varying from 39–41 kDa per subunit (Ohshima & Soda, 1990; Wakayama et al., 2008). These enzymes adapt to various ecological niches by demonstrating different characteristics in terms of kinetic and thermal.

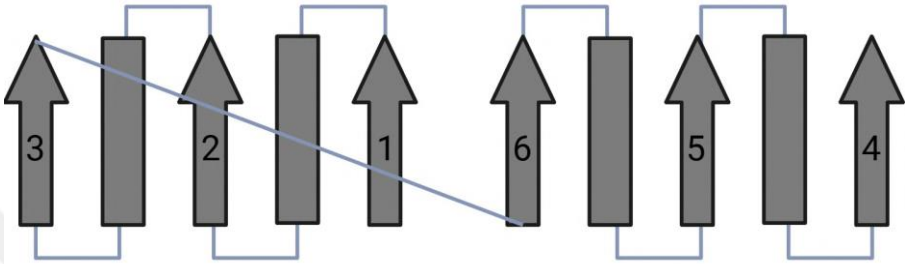

Figure 1.5: Canonical Rossmann fold superstructure assembly in 2D. The β-sheets are represented as arrows and α-helices as rectangle.The β-sheets are flanked by α-helices. The arrows point is significant as the β-sheets oriented as parallels.

1.6.1 Enzymatic Characterization of L-Alanine Dehydrogenase Enzyme Family

The catalytic activity of the L-alanine dehydrogenase varies wildly among the species adapted to different thermal settings. These species of different thermal settings are classified as thermophilic, mesophilic, and psychrophilic. Isolated enzymes from the listed species show different kinetic properties, cofactor affinities, and stability profile. These variations consequently influence the suitability of the enzymes for enzyme engineering and industrial use and are often linked to the ecological niche of the organism.

Thermostable AlaDHs produced from species including *Thermus thermophilus* and *Geobacillus stearothermophilus* show remarkable resilience to denaturation at high temperatures. Often used in industrial operations requiring thermal robustness, these enzymes operate best at temperatures over 60°C (Wakayama et al., 2008). Their thermostability (Kuroda et al., 1989) is attributed in part to structural changes including reduced loop mobility, enhanced hydrophobic core packing, and higher salt bridge generation.

With importance of their metabolic importance, mesophilic AlaDHs—including those

from *Bacillus subtilis*, *Streptomyces spp.*, and *Anabaena cylindrica* are often studied at moderate temperatures (30–37°C). In the case of AlaDH from *B. subtilis*, it has acts as the regulator of sporulation (Siranosian et al., 1993). Applied in metabolic engineering, these enzymes have become references for knowledge of general catalytic behavior (Ohshima & Soda, 1990).

At low temperatures (4–10°C), psychrophilic variations from Antarctic bacteria such *Colwellia* and *Marinomonas* show excellent catalytic efficiency; this is ascribed to enhanced molecular flexibility (Galkin et al., 1999). Less salt bridges, more surface loops, and lower proline content are among the adaptations that improve structural dynamics at cold temperatures but lower general thermal stability (Feller & Gerday, 2003; Galkin et al., 1999).

1.6.2 L-Alanine Dehydrogenase from Vagococcus lutrae

There is not yet any structural or biochemical description of AlaDH from *Vagococcus lutrae* published. Integrating crystallographic analysis, ligand binding investigations, and structural comparison with homologs, this thesis gives the first study of this enzyme. Originally discovered from the common otter (*Lutra lutra*), *V. lutrae* is a catalase-negative, Gram-positive coccus later related to rare incidences of human infections (Lawson et al., 1999; Garcia et al., 2016; Altintas et al., 2020).

Beyond their pathogenicity, *Vagococces* genus members have shown enzymatic potential pertinent to biotechnology. *V. fluvialis*, for instance, has been found to generate a new two-peptide lantibiotic (Salgado et al., 2023), while *V. salmoninarum* codes uridylate kinase, a nucleotide biosynthesis enzyme (UniProt Consortium, 2024). Further underlining the metabolic flexibility within this species, proteolytic enzymes from *V. fluvialis* have also been identified for agrowaste disposal (Ayyam et al., 2025).

V. lutrae has also proven to have the capacity for systemic infection in both animals and humans, implying physiological adaptability and an underestimated metabolic potential even if its isolation is rare. Particularly in the lack of known homologue studies, the functional characteristics of *Vl*AlaDH could shed light on the metabolic functions of this organism and help to define the enzymological scene of AlaDHs.

1.7 Structural Characterization of L-Alanine Dehydrogenases

L-Alanine dehydrogenase (AlaDH) investigated structurally in several bacterial species. This research scope resulted in essential insights into its catalytic mechanisms, cofactor interactions and quaternary assembly. The crystal structures with high resolution have been identified and deposited to Protein Data Bank (PDB) in *Mycobacterium tuberculosis* (PDB ID: 2VHX), *Geobacillus kaustophilus* (PDB ID: 8HYH), and *Phormidium lapideum* (PDB ID: 1PJB) (Ågren et al., 2008; Maeno et al., 2023; Wakayama et al., 1998). These articles helped the foundation of a conserved structural framework for the family of the enzyme. Additionally, it highlighted one of the most common super secondary structures Rossmann fold which carried it function of principal cofactor binding motif carried among the homolog structures (Lesk, 1995; Wakayama et al., 1998). In the PDB, L-Alanine dehydrogenase from *Thermus thermophilus* (PDB ID: 2EEZ) where no written work is associated with the structure in the database. All these structures the continued interest to the enzyme family while showcasing different adaptations to the temperature with thermophiles and mesophiles.

Going through all the structurally characterized AlaDH enzyme, conversation of a highly conserved fold architecture is observed. The main conserved fold among the architecture is Rossmann fold in the N-terminal domain. In this fold, a motif facilitating NAD^+ which follows the following order of GxGxxG. This motif is marked as a hallmark of nucleotide-binding proteins (Lesk, 1995; Wakayama et al., 1998). The location of this motif is generally between the end of the parallel β-sheet continuing towards the α-helices that have flanked. Pyrophosphate moiety of NAD^+ stable bond is established here. The active site is situated in a cleft between two domains, one being the catalytic domain and the other cofactor (NAD^+) binding domain. The domain architecture allows precise alignment of both cofactor and substrate during catalysis (Wakayama et al., 1998; Tripathi & Ramachandran, 2008).

Several AlaDH showed some kind of domain movements upon ligand binding. These domain movements were essential in the function of the enzyme. Notably, when structurally compared, apo and NAD^+ bound *Mycobacterium tuberculosis* AlaDH (PDB ID: 2VHY; PDB ID: 2VHZ) and *Phormidium lapideum* AlaDH (PDB ID: 1PJB; PDB ID:

1PJC) demonstrated unique domain closure upon cofactor binding (Ågren et al., 2008; Wakayama et al., 1998). The movement entails rotation of the catalytic domain toward the Rossmann fold. Rotation results in decreasing the distance between the domains where the substrate binds, improving its alignment as well as the cofactor's (Tripathi & Ramachandran, 2008). The shifting dynamics is essential to the catalyst and has been used to infer functional flexibility of related dehydrogenases not limited to AlaDH (Baker et al., 1998; Maia et al., 2017).

1.8 Amino Acid Dehydrogenases in Biotechnology and Industry

Using NAD^+ or $NADP^+$ as a cofactor, amino acid dehydrogenases (AADHs) are oxidoreductases catalyzed to cause the reversible conversion between amino acids and their corresponding α-keto acids. In industrial biotechnology, their great selectivity, efficiency, and fit for cofactor recycling systems make them indispensable instruments (Knaus et al., 2016).

Among the most often used AADHs are leucine dehydrogenase (LeuDH), phenylalanine dehydrogenase (PheDH), and glutamate hydrogenase (GluDH). Applied in the synthesis of chiral amines, diagnostic biosensors, and cascade reactions are these enzymes LeuDH and PheDH are used in the enantioselective resolution of racemic amines (Knaus et al., 2016), for instance; GluDH is mostly involved in ammonia assimilation and glutamate detection (Chen et al., 2023).

Recent developments include synthetic cofactor nicotinamide cytosine dinucleotide (NCD) (Zhou et al., 2023), modified AADHs with enhanced thermostability and changed cofactor specificity. Furthermore, designed to enable effective amino donor regeneration in sustainable biocatalytic systems are fusion proteins combining AADHs with formate dehydrogenase (Li et al., 2024).

1.8.1 Other Amino Acid Dehydrogenases

Given their substrate selectivity, cofactor compatibility, and catalytic efficiency, certain amino acid dehydrogenases (AADHs) have become rather important for industry. Of these, leucine dehydrogenase (LeuDH), phenylalanine dehydrogenase (PheDH), and glutamate

dehydrogenase (GluDH) stand especially out.

Especially L-tert-leucine, a fundamental intermediary in pharmaceutical production, leucine dehydrogenase (LeuDH; EC 1.4.1.9) is extensively used in the asymmetric synthesis of chiral amino acids. Under fed-batch circumstances, a fresh LeuDH from P*seudomonas balearica* produced effective L-tert-leucine and showed great activity in reductive amination processes (Zhou et al., 2022). Variations with enhanced catalytic efficiency toward bulkier substrates such trimethylpyruvate (Zhou et al., 2023) result from further engineering of LeuDH employing semi-rational design.

Clinically, phenylalanine dehydrogenase (PheDH; EC 1.4.1.20) has found use especially in the monitoring of phenylalanine levels in patients with phenylketonuria (PKU). Potential for point-of-care testing (Luo et al., 2022) is presented by electrochemical biosensors including PheDH into conductive polymer nanostructures showing fast and sensitive detection of L-phenylalanine.

Glutamate dehydrogenase (GluDH; EC 1.4.1.2) catalyzes the oxidative deamination of L-glutamate to α-ketoglutarate, therefore playing a key part in nitrogen metabolism. Under ammonium-rich circumstances, GluDH is a fundamental enzyme for ammonia assimilation in nitrogen-fixing bacteria such *Bacillus macerans*, therefore promoting cellular nitrogen balance (Goldberg et al., 1969).

Supporting uses from chiral amine synthesis to biosensor creation and metabolic engineering, these AADHs highlight the variety and use of dehydrogenases in industrial biotechnology.

1.8.2 L-Alanine Dehydrogenase

With NAD^+ as a cofactor, L-alanine dehydrogenase (L-AlaDH; EC 1.4.1) catalyzes the reversible conversion of pyruvate and ammonia to L-alanine. It serves in redox homeostasis and nitrogen metabolism in bacteria. For industrial L-alanine manufacture, its great specificity and compatibility with cofactor recycling systems make it a useful biocatalyst (Dave & Kadeppagari, 2019).

Recent comparative investigations of L-AlaDH enzymes from *Bacillus* species, *Mycobacterium smegmatis*, and *Geobacillus stearothermophilus* have shown clear variations

in enzymatic qualities fit for different uses (Gu et al., 2023). Key conformational changes observed in crystallographic investigations including those on Mycobacterium tuberculosis L-AlaDH following NAD^+ binding underpin their catalytic function (Ågren et al., 2008).

L-AlaDH has also been added to formate dehydrogenase in NADH-regenerating systems to facilitate effective amino acid production. These methods provide sustainable paths for industrial L-alanine manufacture as well as increase conversion rates (Gu et al., 2023). Although various homologues have been structurally defined, the L-AlaDH enzyme from *Vagococcus lutrae* has not yet been investigated. By means of the first structural and functional analysis of VlAlaDH, this thesis expands the knowledge of this enzyme class.

1.9 Molecular Docking

Molecular docking is a computational application used to predict the orientation preferred by the small molecule bound to the protein target. By simulating the orientation, binding affinity and identification of key interactions is possible to be estimated at the atomic level (Morris & Lim-Wilby, 2008). It's valuable when the molecule investigated has no ligand-protein complex available. Docking simulations therefore can provide insights into potential binding modes, catalytic residues, and ligand accessibility (Lengauer & Rarey, 1996).

In this study molecular docking was done to identify the interactions between protein *Vagococcus lutrae* L-Alanine Dehydrogenase (*Vl*AlaDH) and its physiological ligands and their derivatives including, L-alanine, pyruvate, α-ketobutyrate, α-ketovalerate, α-ketocaproate. The rationale behind the selection of these keto acids was their biochemical relevance and previously documented activity with other alanine dehydrogenases. For the case of documented activity with other dehydrogenases, enzymes from Bacillus subtilis namely L-Alanine dehydrogenase have been shown to utilize α-ketobutyrate and α-ketocaproate as alternative substrates (Pietruszko et al., 1965). For the biochemical relevance for biotechnology would be, α-ketovalerate has been tested in microbial fermentation pathways for biofuel production (Wang et al., 2023).

The structure determined in this study apo crystalline structure, docking done in silico served crucial purpose of identifying the enzyme's substrate binding sites. Docking went through with the server CB-Dock2, a blind docking server that uses cavity detection and AutoDock Vina scoring to identify favorable ligand binding pocket and orientation (Liu et al., 2020).

1.10 X-ray Crystallography

X-ray crystallography is one of the most widely used methods for determining the three-dimensional structures of proteins. The method works with shooting X-rays at a protein crystal and diffracted rays analyzed in the form of diffraction pattern. These patterns give us the necessary information of how the atoms are arranged in the protein. The diffraction later transformed into an electron density map where researchers model the positions of each atom to understand the protein structure in detail (Drenth, 2007; Glusker et al., 1994).

To go forward with this method, high quality protein crystals need to be obtained. Crystallization is achieved when the protein molecule in solution becomes supersaturated, which means protein is more concentrated than the solubility limit. Nucleation is the process where small, ordered clusters of protein molecules begin to form. Nucleation follows thermodynamic imbalance resulting from supersaturation (Figure 1.6). The clusters formed during the nucleation later grow into larger crystals as more protein molecules join the lattice. The process of crystallization is sensitive due to factors affecting the precipitation which are pH, salt concentration, temperature, and the type of precipitant (McPherson & Gavira, 2014).

In this study, selected protein crystallization method was the microbatch under oil where the protein and screening conditions have been mixed in the wells of Terasaki plates and covered with paraffin oil. By using paraffin oil, evaporation has been prevented thus allowing slow and stable equilibration. Following this crystallization protocol makes the crystallization suitable for sensitive proteins and room-temperature setups. It also standardizes the crystallization process allowing high-throughput screening of many conditions in a compact and efficient format (Ertem et al., 2022).

Once crystals are formed, each of them grouped based on their specific space group

which describes how molecules are arranged in the crystal. How the unit cell is repeated, and the structure is solved depends on the molecular arrangement that creates the symmetric properties of the crystal. Space group information gives the structural biologist help define the interaction of the molecules within the crystal formation and how it is assembled in the biological systems. (Glusker et al., 1994; Drenth, 2007). Although the number of solved structures is limited, the observed space groups are varied. These include examples for trigonal from *Phormidium lapideum* L-alanine dehydrogenase (PDB ID: 1PJB; Wakayama et al., 1998) and for monoclinal from *Mycobacterium tuberculosis* L-alanine dehydrogenase (PDB ID: 2VHX; Agren et al., 2008). Observed diversity in the space group reflects differences in molecular packing, domain flexibility, and crystallization conditions among homologs.

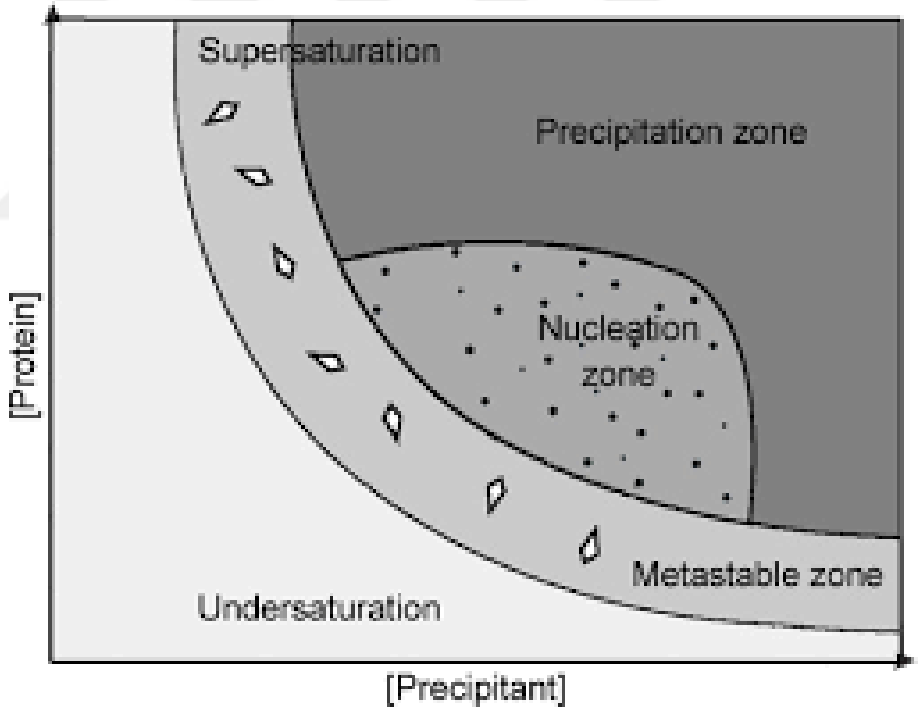

Figure 1.6: Protein crystallization phase diagram.

Chapter 2

MATERIALS AND METHODS

2.1 Materials and Equipments

2.1.1 LB Medium, Stock Antibiotics and IPTG

LB medium (Table 2.1) and stock solutions of antibiotics and 0.4 M IPTG (Table 2.2) have been prepared for use in transformation and protein expression experiments.

Table 2.1: LB Medium

Reagent	**Amount (g/L)**
Tryptone	10
NaCl	10
Yeast extract	5
Total	25

Table 2.2: Antibiotic and 0.4 M IPTG Stock Solutions

Reagent	**Amount (mg/ml)**
Kanamycin	50
IPTG	95.324

2.1.2 Buffers

A pH level of 7.5 has been utilized in the preparation of lysis buffer (Table 2.3), HisA buffer (Table 2.4), and HisB buffer (Table 2.5) for the purpose of conducting protein purification and checking the expression of proteins on a smaller scale.

Table 2.3: Lysis Buffer

Reagent	**Final concentration**	**Amount**
NaCl	500 mM	29.22 g
Tris	50 mM	6.06 g
Glycerol	5% (v/v)	50 ml
Triton X-100	0.5% (v/v)	5 ml
Imidazole	20 mM	1.362 g
ddH_2O	—	up to 1 L
Total	—	**1 L**

Table 2.4: HisA Buffer

Reagent	**Final concentration**	**Amount**
NaCl	200 mM	11.688 g
Tris	20 mM	6.06 g
Imidazole	20 mM	1.362 g
ddH_2O	—	up to 1 L
Total	—	**1 L**

Table 2.5: HisB Buffer

Reagent	**Final concentration**	**Amount**
NaCl	200 mM	11.688 g
Tris	20 mM	6.06 g
Imidazole	250 mM	17.019 g
ddH_2O	—	up to 1 L
Total	—	**1 L**

2.2 Preparation of Glycerol Stocks

Already transformed have come from Prof. Dr. Barış Binay, Gebze Technical University in the agar plate with colonies have been selected by kanamycin antibiotic resistance. The plasmid used for the transformation of ald gene was pET-28a(+) (Figure 2.1). The constructs are included with non-cleavable C-terminal hexahistidine for affinity chromatography. The sequence of the protein can be found below. Hexahistidine tag can be seen as bold characters.

Wild-type VlAlaDH:

MIIGIPKEILDNENRVALTPVGVEAFLKQGHEVRVEKNAGEGSGFTDD
AYEAAGAILSDDPAFVWQADMVMKVKEPKPSEYHYFRENLILFTYLH
LAPATELTQALIDAKVTAIAYETIQLEDRSLPLLIPMSEIAGRMSVQIGA
QLLEKSKGGKGILLAGIPGVKKGNVVIIGGGNVGTNAAKIAIGLGANV
TILDVNQKRLAELDALFGNEIQTLISNAHNIAETVKTADVVIGTVLIPGA
KAPTLVTEEMVASMGEGSVIVDVAVDQGGIFETIDHVTSHSNPTYVRHG
VIHYAVPNMPGNVARTSTIALTNATLPYAMQMATHDLNDVLRQTPSLQKGVN
IYQGVLTNEQIAAAQN RKFQQLAKLIGEHHHHHH

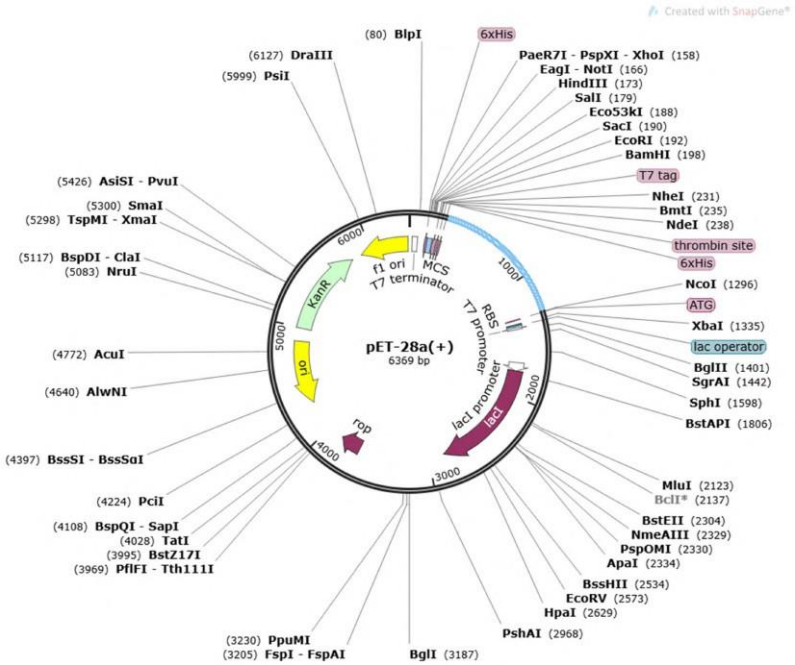

Figure 2.1: The plasmid map of pET-28a(+) vector used for bacterial expression. KanR indicates the kanamycin resistance gene. (Gene Universal, USA).

10 mL of LB medium sterilized at 121°C for 20 minutes using an autoclave. 10 µL of kanamycin antibiotic was included into the LB medium before the transfer, as the pET-28a(+) vector confers resistance to kanamycin, facilitating the proliferation of the bacteria harboring the vector. The colonies on the agar plate have been scraped with a microtip and inoculated into the LB medium. The inoculated culture was thereafter cultured in an incubator at 37 °C and 110 rpm for 18-20 hours overnight.

To prepare glycerol stock for preliminary expression assessment and subsequent protein expression, the incubated LB medium was partitioned into 750 µL aliquots, to which 750 µL of 80% sterile glycerol was added, resulting in five tubes of glycerol stock.

2.3 Smale Scale Expression Check

10 milliliters of LB medium have been prepared for the protein of interest, wild-type VlAlaDH, and the LB has been sterilized by autoclaving at 121°C for 20 minutes. 10 µL of kanamycin (100 mg/mL) antibiotics have been included into the LB medium. Final concentration will be 100 µg/mL.

The glycerol stock of the wild-type VlAlaDH construct has been inoculated into the prepared media. The construct was incubated in LB media at 37 °C with continuous shaking at 110 rpm for a duration of 18 to 24 hours. Following overnight incubation, 3 mL was reserved for cell collection via centrifugation. The supernatant obtained from centrifugation was discarded. The collected cells were stored in a -45 °C refrigerator for subsequent use in a pulldown experiment.

Prior to the induction process, the incubator was cooled to 30 °C. The induction was performed by adding 7 µL of 0.4 M IPTG (isopropyl β-D-1-thiogalactopyranoside) to the residual culture. The ultimate concentration will be 0.4 mM. The cultures were incubated overnight (18-24 hours) at 30 °C and 110 rpm. Upon completion of induction, the cells in the residual media were collected using centrifugation at 3500 rpm for 30 minutes.

The cell pellets were resuspended using the lysis buffer (refer to Table 2.3) and subjected to sonication until liquefaction occurred. The prepared cell lysate was subsequently subjected to centrifugation at 10,000 rpm for 15 minutes. The supernatants obtained from centrifugation were transferred to clear tubes. 40 µL of Ni-NTA beads were added to each

clear tube. The supernatant and bead-containing tubes were incubated at +4 °C overnight for a duration of 18 to 24 hours.

The pull-down experiment was conducted after centrifugation of the supernatant bead-containing tube at 2400 rpm for 2.5 minutes. The remaining supernatant was carefully pipetted into another tube.

1 mL of HisA buffer (see Table 2.4) was added to the tube and incubated on ice for 30 minutes. The samples underwent centrifugation at 2400 rpm for 2.5 minutes, after which the supernatants were discarded. Two hundred microliters of HisB buffer (see Table 2.5) were added to the tube and incubated for 2 to 3 minutes to elute the protein from the beads.

2.4 Large-scale Protein Production and Purification

200 mL and 4 x 1.5 L of LB media were prepared and subsequently autoclaved for sterilization. A stock solution of kanamycin, totaling 150 µL, has been incorporated into 200 mL of LB medium. Cells were extracted from the glycerol stock at -80°C using a micropipette tip and subsequently inoculated into LB medium. The inoculation precedes the incubation of the LB medium at 37 °C and 110 rpm for a duration of 18 to 24 hours.

On the subsequent day, 1.5 mL of kanamycin was added to each 1.5 L of LB medium. The overnight growth was divided into four portions, with each portion added to 1.5 L of LB medium, incorporating 50 mL of the preceding culture. 1.5 L LB mediums are reintroduced into the incubator at 37 °C and 110 rpm for a period of 18 to 24 hours. The LB medium monitored the optical density at 600 nm (OD600) of the culture every hour using a Nanodrop device (Thermo Fisher, USA). Upon reaching an OD600 of 0.7-0.8, 1.5 mL of IPTG is added for induction once the incubator temperature has cooled to 30 °C. The cultures were left overnight following induction.

Following incubation, the cultures underwent centrifugation at 3500 rpm for 45 minutes, after which the supernatants were removed. Most of the cells were collected from the centrifuge bottles with a spoon and subsequently transferred into falcon tubes. The remaining cells were obtained by dissolving into several milliliters of LB. The falcon tubes were centrifuged at 3500 rpm for 30 minutes, after which the supernatants were discarded. The harvested cell pellets were maintained at -45°C prior to purification.

When it comes to purification period, a big box has been filled to the top with crushed ice. Lysis buffer (refer to Table 2.3) was added to the cell pellets until the volume reached 45 ml in the falcon tube. The cells underwent sonication done 1 second on and 1 second off for 30 seconds at 60% amplitude. The protocol was reiterated until the pellets were fully dissolved. To prevent overheating, the samples were incubated on ice during sonication intervals.

After sonication, the cell lysates were transferred to ultracentrifuge tubes and balanced using a weighing device. Cell lysates underwent ultracentrifugation using a Ti45 rotor in a Beckman Optima TM L-80XP Ultracentrifuge (Beckman, USA) at 35,000 rpm for 1 hour and 15 minutes at 4°C. Upon completion of ultracentrifugation, the supernatants were collected and filtered through filter paper to yield a purified solution.

An AKTA-Go FPLC device was utilized for protein purification. The supernatant was applied to a Ni-NTA affinity column connected to an AKTA go system. The initial step involved equilibrating the Ni-NTA column with HisA wash buffer (see Table 2.4) until stabilization of UV absorbance was achieved. Following the equilibration of the column, the complete supernatant was introduced into the column, and the flowthrough, containing unbound proteins, was collected from the outlet valve. Subsequently, the column was washed with His A buffer to remove unbound and nonspecifically bound proteins, continuing until the UV absorbance stabilized. Upon achieving stable UV absorbance, the HisB elution buffer (see Table 2.5) was introduced to the column to elute L-Alanine Dehydrogenase from *Vagococcus lutrae*. The eluted protein was concentrated using a 30 kDa Amicon Ultra centrifugal filter tube.

2.5 Protein Crystallization

The crystallization method employed was sitting drop microbatch under oil for L-Alanine dehydrogenase from *Vagococcus lutrae*, utilizing 3500 commercially available sparse matrix crystallization screening sets. 0.83 µL of protein solution was combined with 0.83 µL of crystallization solution in the wells of 72-well Terasaki plates (Figure 2.2). Each well received approximately 16.6 µL of paraffin oil as a cover. Approximately 3,500 crystallization conditions were screened twice at the ambient temperature and at +4 °C.

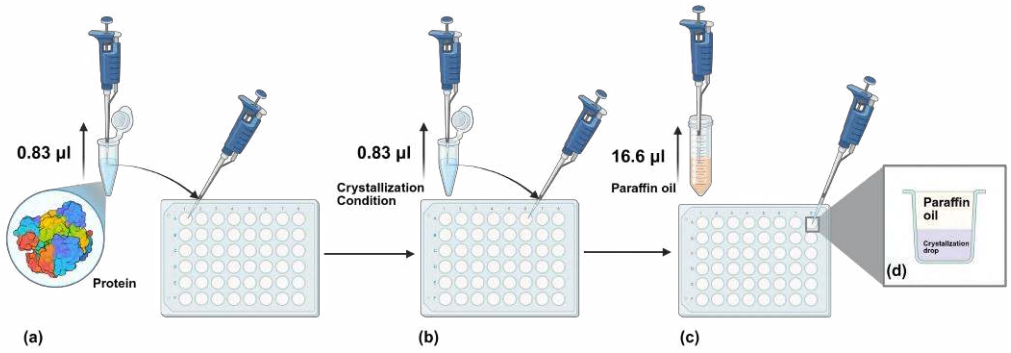

Figure 2.2: Sitting drop vapor diffusion microbatch under oil method. (a) 0.83 µL of protein solution has been pipetted to the 72-well Terasaki plate. (b) 0.83 µL of crystallization condition has been pipetted and mixed with the protein solution. (c) The well has been closed down with paraffin oil.

The *Vl*AlaDH protein crystals were obtained in a crystallization solutions Wizard Classic Condition I #37 consisted of 250 mM Sodium chloride, 100 mM Imidazole/ Hydrochloric acid pH:8.0 (Rigaku, Japan), Salt RX I #29 consisted of 2.0 M Sodium formate, 0.1 M TRIS pH:8.5, Salt RX I #32 consisted of 3.5 M Sodium formate, 0.1 TRIS pH:8.5 (Hampton Research, USA) and Helix I#5 consisted of 0.1 M Lithium Chloride, 0.01 M Manganese (II) chloride tetrahydrate, 0.05 M MES pH:6.5, 25% v/v PEG 400 (Molecular Dimensions, UK). The said crystals were from the crystallization batch of ambient temperature crystallization. The crystallization experiments were replicated under identical conditions across all wells of a Terasaki plate to obtain additional crystals.

2.6 X-ray Data Collection and Processing

X-ray crystallographic data were collected utilizing the Rigaku XtaLAB Synergy Flow X-ray Diffractometer at the Turkish Light Source (University of Health Sciences, Istanbul, Türkiye). The Oxford Cryosystems Cryostream 800 Plus was calibrated to 300 °K for the collection of ambient temperature data. The Terasaki plate was affixed to the XtalCheck-S

plate reader (Gul et al., 2023), facilitating the screening of multiple crystals within the Terasaki plate. Following the screening of all crystals, those exhibiting good diffraction properties were selected. The data collected from three crystals. The detector distance was established at 100.00 mm. Diffraction data were obtained from a single crystal with a 5-second exposure duration and a 1.00-degree oscillation. The plate oscillated to a total of 22.5 degrees.

The ambient temperature data was handled with the automatic data reduction feature in CrysAlis Pro software, resulting in the generation of an mtz file. Each segment of the ambient temperature data has been reviewed by peak detection and masking, with unsuitable unit cells being manually eliminated. The xx proffitbatch command was executed in the command shell to generate a batch script for cumulative data reduction. The batch script was executed by entering script in the command shell. Each data reduction produced a rrprof file with all unmerged and unscaled data. The profit merging tool integrated into CrysAlis Pro was utilized to amalgamate all the decreased data and export an MTZ file.

2.7 Structure Determination and Refinement

Molecular replacement for the apo- *Vl*AlaDH structure was performed automatically via molecular replacement module in the PHASER (McCoy et al., 2007) found in the PHENIX software package. For MR process, the initial search model is predicted AlphaFold (Jumper et al., 2021) model from the AlphaFold DB (Varadi et al., 2022). The model generated from the full length wild-type monomer sequence where it was retrieved from UniProt Database (The UniProt Consortium, 2015) (UNIPROT ID: V6QCH) and built as a monomer and downloaded as PDB file. No further modification nor truncation done to the model.

The initial rigid-body and simulated annealing refinements were conducted using PHENIX, utilizing the model coordinates as a basis. Subsequently, individual coordinates and translation/libration/screw (TLS) parameters underwent refinement using PHENIX. The refined model underwent verification using COOT (Emsley and Cowtan, 2004) following each refinement run. The modified side chains and water molecules that were

absent from the electron density were corrected manually. Water molecules exhibiting no or negative density were eliminated.

The structural alignments were performed using PyMoL. The root-mean-square deviation (RMSD) scores were calculated based on the alignment of Ca atoms. The figures were produced using PyMoL, COOT, LigPlot+ (Laskowski and Swindells, 2011), and BioRender.

2.8 Generating Phylogenetic Tree

AlaDH sequences were retrieved of 13 unique organisms from UniProt and aligned using Clustal Omega (EMBL-EBI) (Sievers & Higgins, 2014). Based on this alignment, the phylogenetic tree was generated in Newick format and visualized using Interactive Tree of Life (iTOL) (Letunic & Bork, 2021). The detailed list of the structures used, and their structural availability is shown below (Table 2.6).

Table 2.6: Sequences used for generating the phylogenetic tree

Source Organism	**UniProt ID**	**Structure Available**	**PDB IDs**
Amylobacter fermentans	A0A3Q9HQQ2	No	
Bacillus subtilis	Q08352	No	
Caulobacter henricii	A0A0P0NW57	No	
Corynebacterium phoce	A0A1L7D1K5	No	
Geobacillus kaustophilus	Q5KW99	No	8HYE, 8HYH
Halomonas elongata	E1V931	No	
Mycobacterium tuberculosis	P9WQ81	Yes	2VHW, 2VHW, 2VHX, 2VHY, 2VHZ
Phormidium lapideum	O52942	Yes	1PJB, 1PJC, 1SAY
Pseudarthrobacter equi	A0A1H1SIE3	No	
Spirosoma lodoensis	A0A7L5DTX5	No	
Staphylococcus aureus	Q2FH00	No	
Stenotrophomonas rhizophila	Q5SLS7	Yes	2EEZ
Vagococcus lutrae	V6QCH9	No	

2.9 Molecular Docking

Molecular docking simulation is carried out to evaluate the binding mechanism of the main substrates of the AlaDH which are pyruvate and L-alanine, alongside the related keto-acids to pyruvate. The apo-crystal structure of *Vl*AlaDH that has been determined in this study is used as the base model for docking. Included as pyruvate, alanine, α-ketobutyrate, α-ketovalerate, and α-ketocaproate have downloaded as SDF format to be used for docking.

Template based blind docking was carried out via the webserver CB-Dock2 (Liu et al., 2022), which automatically detects the most probable ligand-binding pocket location based on the alignment halo homolog enzymes. These are called templates in the webserver where the model is going to be docked aligned to these templates. The templates for each ligand included were *Phormidium lapideum* AlaDH (PDB ID: 1SAY) and *Mycobacterium tuberculosis* AlaDH (PDB ID: 2VHX). The docking algorithm used FitDock scoring to rank the probable pockets.

The results of the docking process are illustrated in the 3D space with PyMol (Schrödinger, LLC). To inspect the interaction of the ligands in the 2D plane LigPlot+ (Laskowski & Swindells, 2011) used to generate graphs identifying the hydrogen binding residues and the hydrophobic interacting residues and identify key active site residues.

Chapter 3

RESULTS

3.1 Expression of Wild-type VlAlaDH

The transformed *E. coli* strain BL21(DE3) was cultivated in numerous colonies on an agar plate with kanamycin, indicating successful transformation. To control the success of the growth of the selected colony which carries our gene of interest, which is ald gene to synthesize *Vl*AlaDH, small-scale expression and pulldown assay was done before large-scale production.

The result comes from the small-scale expression done to show successful overexpression of *Vl*AlaDH by BL21(DE3) with IPTG induction at 30°C for overnight which would be 20 hours. The resulting band after the induction called "after-induction" exhibited a thick band of the size of around 40 kDa, whereas it wasn't visible in the "before-induction" sample.

After achieving positive results in the previously done small-expression check, wild-type *Vl*AlaDH constructs in the 6L of LB medium at the same conditions with the small-scale expression check. We were able to obtain high concentration of wild-type *Vl*AlaDH (Figure 3.1). The monomeric form appears in the gel as a thick band in two lanes with around 40 kDa in size.

During the purification process to make the eluted protein not be kept inside the flowthrough, we went with two steps of injection of the sample to the Ni-NTA column. In the pellet there's not much visibility of any bands since the pellet lysis process wasn't carried out thoroughly. In the eluted samples in the gel, we can also observe some impurities, but they have been gotten rid of by concentration methods with specific weight limit of molecules.

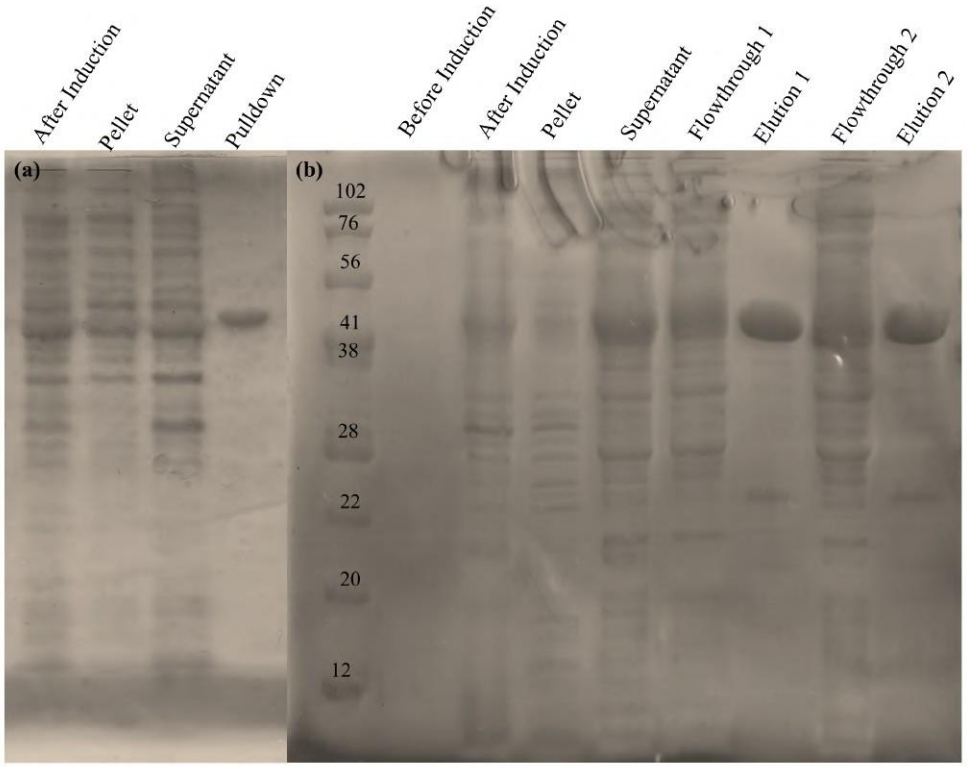

Figure 3.1: The SDS-Page gels of small-scale expression check and large-scale expression. (a) Small-scale expression check (b) Large-scale expression. Each lane content is written on top of the lane.

3.2 Crystallization of Wild-type VlAlaDH

The crystallization process of wild-type has been carried out with the microbatch under oil technique. The protein has been screened by approximately 3500 premixed conditions. The screenings were done to be kept in +4°C and room temperature. The crystals were obtained in the room temperature condition (Figure 3.2). The crystals that have been collected were from Wizard Classic Condition I #37 (Rigaku, Japan) consisted of 250 mM Sodium chloride, 100 mM Imidazole/ Hydrochloric acid pH:8.0, Salt RX I #29 (Hampton Research, USA) consisted of 2.0 M Sodium formate, 0.1 M TRIS pH:8.5, Salt RX I #32 (Hampton Research, USA) consisted of 3.5 M Sodium formate, 0.1 TRIS pH:8.5 and Helix I #5 (Molecular Dimensions, UK) consisted of 0.1 M Lithium Chloride, 0.01 M Manganese (II) chloride tetrahydrate, 0.05 M MES pH:6.5, 25% v/v PEG 400.

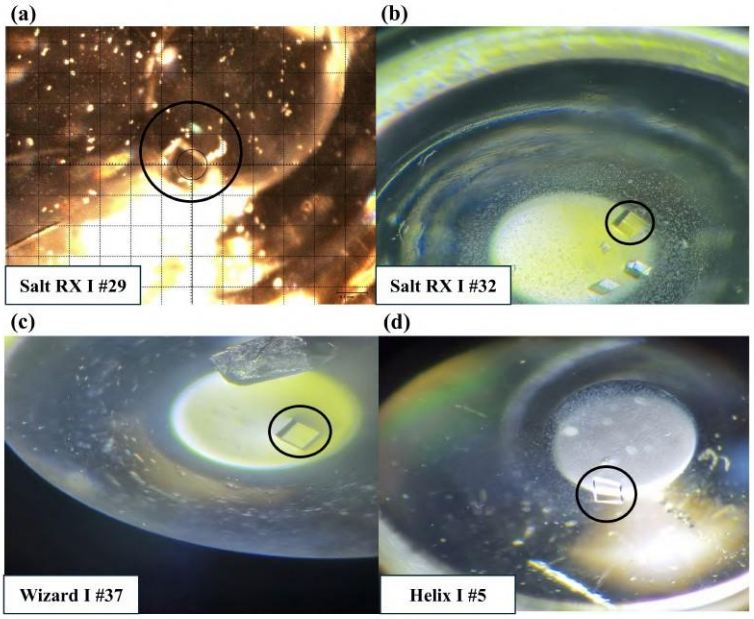

Figure 3.2: *Vl*AlaDH under microscope and in the frame viewer. The crystals that have been used for data collection have been circled by black circles. The bottom left of every panel has the condition name where the crystals have been formed.

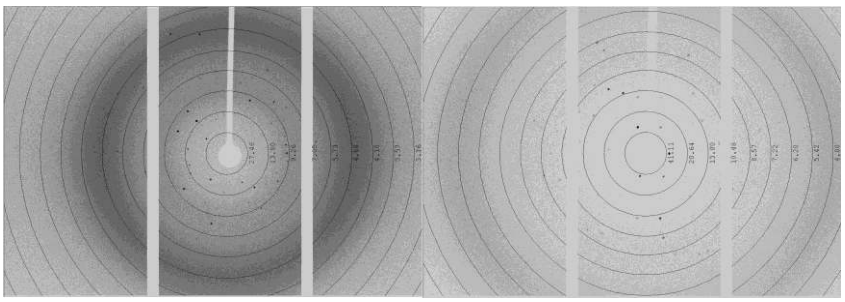

Figure 3.3: Example diffraction pattern screenshots while collecting used for data processing.

3.3 3.3 Structural Analysis of Wild-type VlAlaDH

3.3.1 Ambient Temperature Structure of Wild-type Apo VlAlaDH Structure at 3.2 Å Resolution

The crystal structure of wild-type apo *Vl*AlaDH was elucidated at a resolution of 3.2 Å under ambient temperature conditions (Figure 3.4). The crystallographic asymmetric unit has a solitary monomer, but the biological assembly is hexameric. Secondary structure elements are distinctly colored to enhance the clarity of the functional motifs. The crystals are classified under the hexagonal space group H 3 2, identical to that of the *Phormidium lapideum* AlaDH structure (Baker, et al., 1998), indicating a conservation of molecular conformation and packing attributes among the homologs. The overall completeness of the structure would be 97.8%. The Ramachandran Plot shows 81.87% residues are in the favored region, and only 5 residues are in the disallowed region which makes it 1.37%. The data refinement statistics and data collection statistics can be found in the following Table 3.1.

Table 3.1: Wild type *Vl*AlaDH ambient data collection and refinement statistics

Dataset	VlAlaDH-Ambient
PDB ID	-
Data collection	
X-ray source	Turkish DeLight
Temperature (K)	298
Space group	H 3 2
a, b, c (Å)	115.34, 115.34, 199.46
α, β, γ (°)	90.00, 90.00, 120.00
Resolution (Å)	30.10-3.22
CC1/2	0.939
CC*	0.984
$I/\sigma I$	4.06
Completeness (%)	97.8
Refinement	
Resolution (Å)	30.10-3.22 (3.29-3.22)
No. reflections	8,346
Rwork / Rfree	0.20/0.31
No. atoms	
Protein	2730
Ligand / Ion / Water	11
B-factors	
Protein	118.8
Ligand / Ion / Water	77.5
Coordinate error (Å)	
Bond lengths (Å)	0.0149
Bond angles (°)	2.8650
Ramachandran plot	
Favored (%)	81.87
Allowed (%)	16.76
Disallowed (%)	1.37

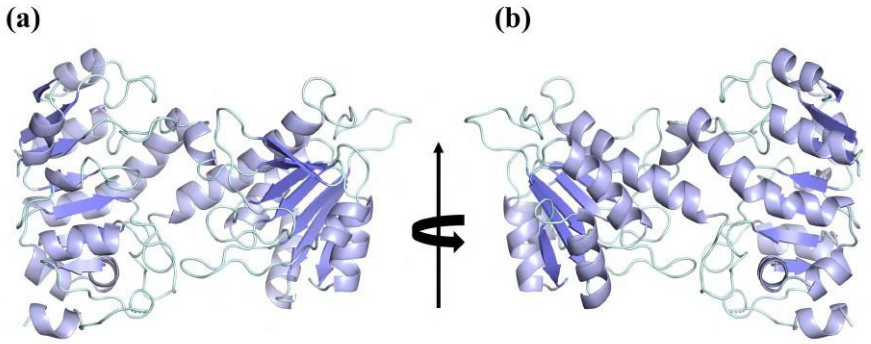

Figure 3.4: 3.2 Å resolution shown as monomer being its asymmetric unit (ASU). (b) is the form of 180° turn in the y-axis of (a). Each secondary structural element has been colored differently. α-helices colored as light blue, β-sheets colored as slate, and the loop regions colored as pale cyan.

The PISA analysis indicated that the hexameric assembly of wild-type *Vl*AlaDH (Figure 3.5) possesses a buried surface area (BSA) of approximately 18,700 Å^2, whereas the dimer interface is approximately 3,250 Å^2 (Krissinel & Henrick, 2007). Given that BSAs exceeding 2,000 Å^2 generally signify stable assemblies (Janin et al., 2008), the hexamer presumably constitutes the predominant biological form. The prominent dimeric interface indicates that the hexamer may disassociate into stable dimers under specific conditions.

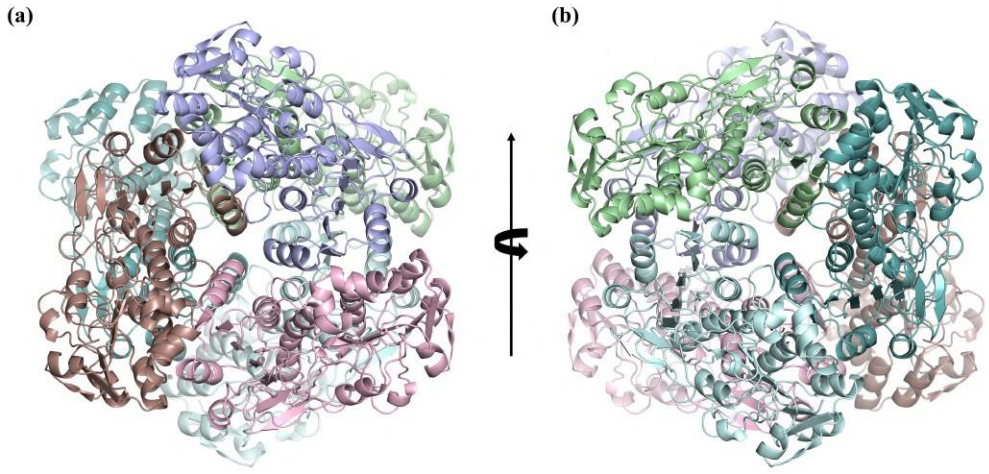

Figure 3.5: Biological assembly shown as homo-hexamer of *Vl*AlaDH. (b) is the form of 180° turn in the y-axis of (a). Each chain has been colored differently.

The monomer comprises two principal functional units and one supplementary unit. The two functional units are super secondary structures referred to as Rossmann folds, characterized by the essential architecture of β-α-β motifs (Hanukoglu, 2015). The C terminal Rossmann fold encompasses the active site residues, seen in light blue, spanning residues 1-129 and 300-371. C-Terminal Rossmann fold gets flanked with the connector helix and N-terminal Rossmann fold. The N-terminal Rossmann fold functions as the principal anchoring site for NAD^+ /NADH, depicted in light orange, encompassing residues 150-300. An α-helix links the two Rossmann folds (Figure 3.6).

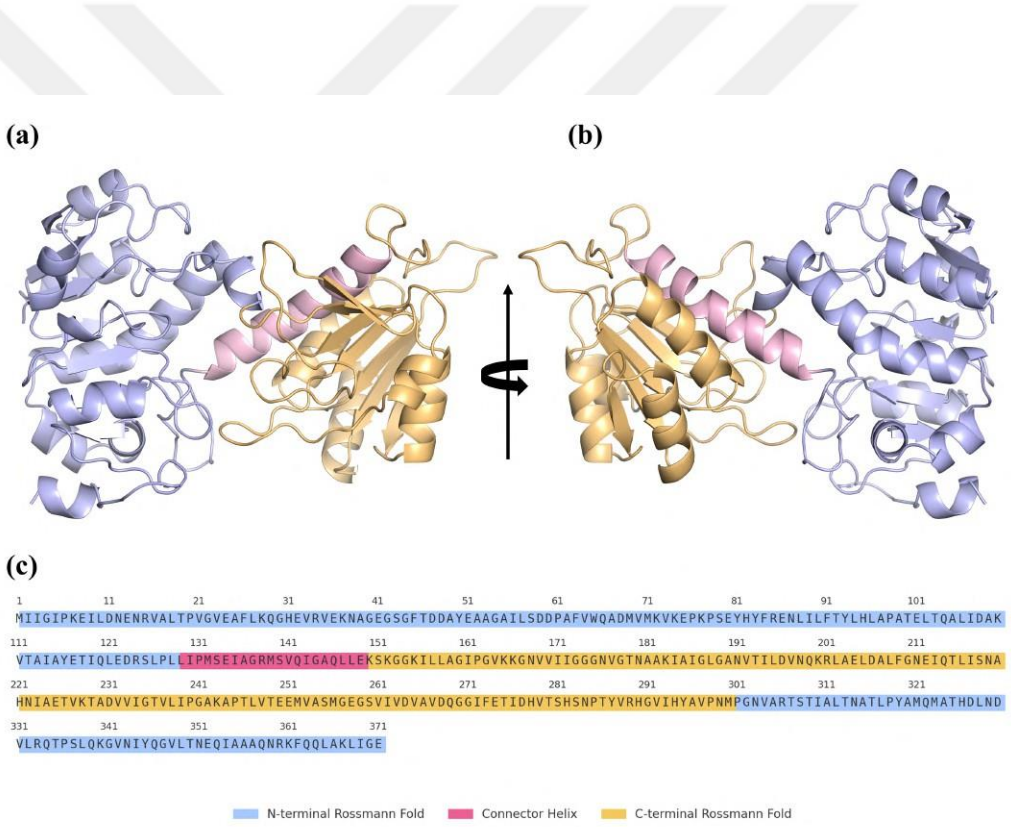

Figure 3.6: Monomer structure divided into functional and companion units. Each motif has been colored differently. (a) Face representation of the motifs. (b) 180°-degree rotation of the face representation. (c) The color-coded map of the residues numbers according to their motif.

3.3.2 Comparison of Apo VlAlaDH Structure with Sequence Based Prediction by Alpha Fold

AlphaFold (Jumper et al., 2021) has been used as the template model for the molecular replacement process. The prediction generated the subsequent model (Figure 3.7). The confidence level of each segment of the protein is apparent. The model demonstrates robust per-residue confidence and a predicted template modelling (PTM) value of 0.98, indicating high overall model confidence.

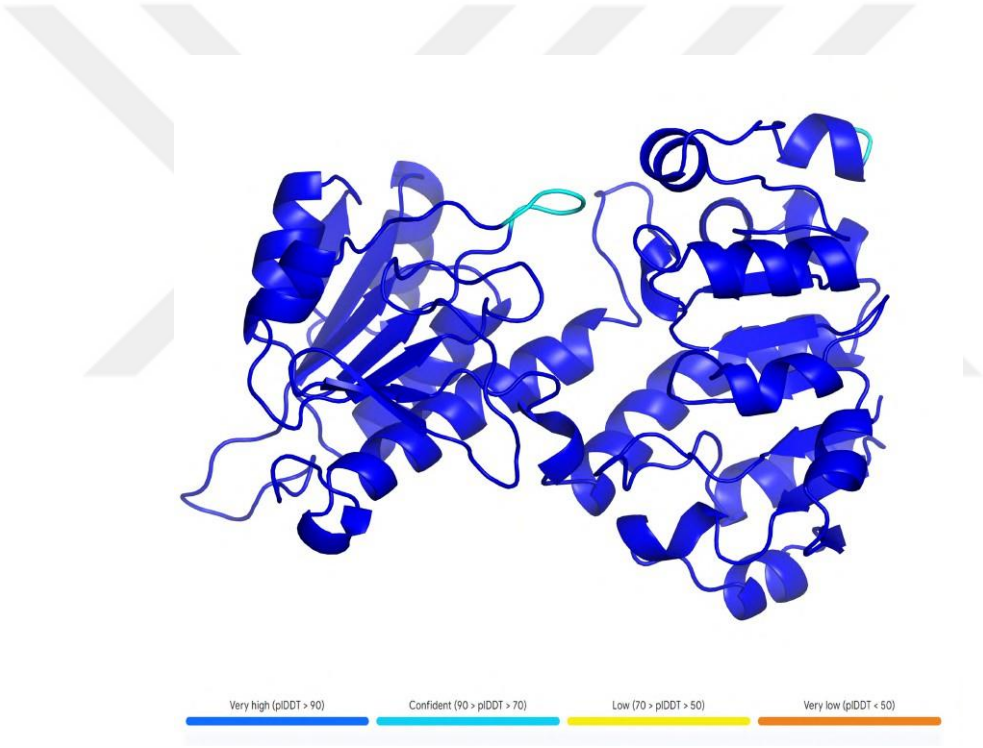

Figure 3.7: AlphaFold-predicted structure of *Vl*AlaDH colored by pLDDT confidence score. Very high confidence regions are shown in dark blue, and lower confidence loops in cyan.

Comparison done with the experimentally uncovered structure of *Vl*AlaDH done based on the previously described motifs (Figure 3.6), which are N-terminal Rossmann fold, C-terminal Rossmann fold, Connector Helix and All the motifs were aligned based on C_α atoms of each residue (Figure 3.8).

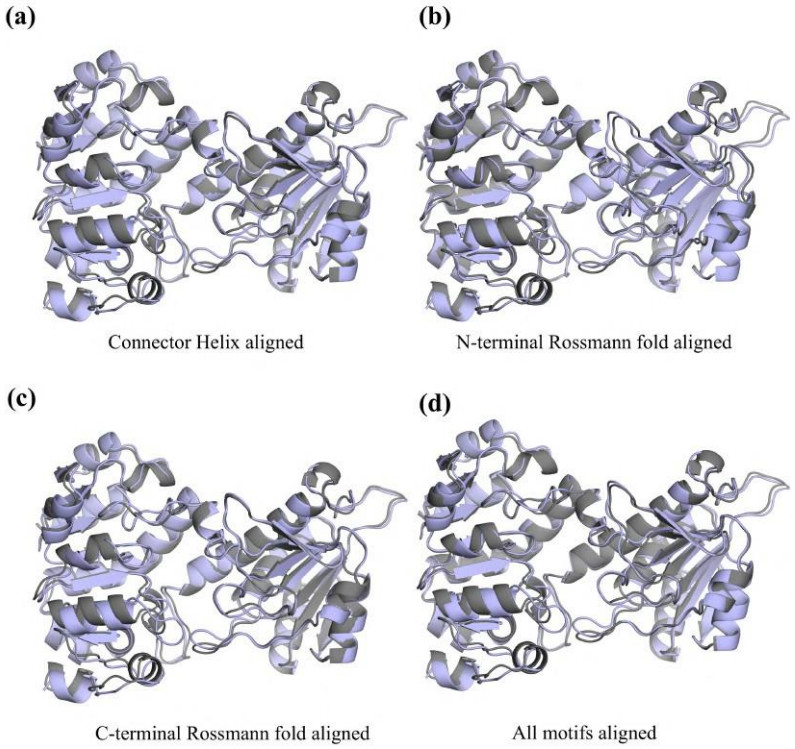

Figure 3.8: Comparison of experimental model, colored light blue, and predicted model, colored grey. (a) Alignment based on connector helix (residues 129-149), (b) alignment based on N-terminal Rossmann fold (residues 1-128 and 301-371), (c) alignment based on C-terminal Rossmann fold (residues 150-300), and (d) alignment based on all the motifs (N-terminal Rossmann fold, C-terminal Rossmann fold, connector helix)

The alignment of the N-terminal Rossmann fold (residues 1-129 and 301-371) yielded an RMSD value of 0.547 Å. This value signifies a structurally analogous entity that is not a complete one-to-one replica. Although the disparity between the structures is predominantly confined to loop regions, the secondary structures remain preserved. The subsequent alignment of the C-terminal Rossmann fold (150-300) yielded an RMSD value of 0.386 Å. The value was lower than the other Rossmann fold alignment. This once more involved the transformation of secondary structural elements, which is essential to the Rossmann fold mechanism. The connector helix (130-149), between these two Rossmann folds in each end, exhibited the lowest RMSD value of 0.400 Å. This once more demonstrated the complete alignment of the helixes without difficulty. All of the motifs based RMSD computed as 0.641 Å.

3.3.3 Comparison of Apo Structures with Homolog AlaDH Structures

In order to see the structural differences a comparison based on previously described motif (Figure 3.6). Two of the homologs, *Phormidium lapideum* and *Mycobacterium tuberculosis*, was compared visually.The remaining homologs with the ones compared visually, RMSD values result of alignment are all visualized as heatmap grid (Figure 3.9).

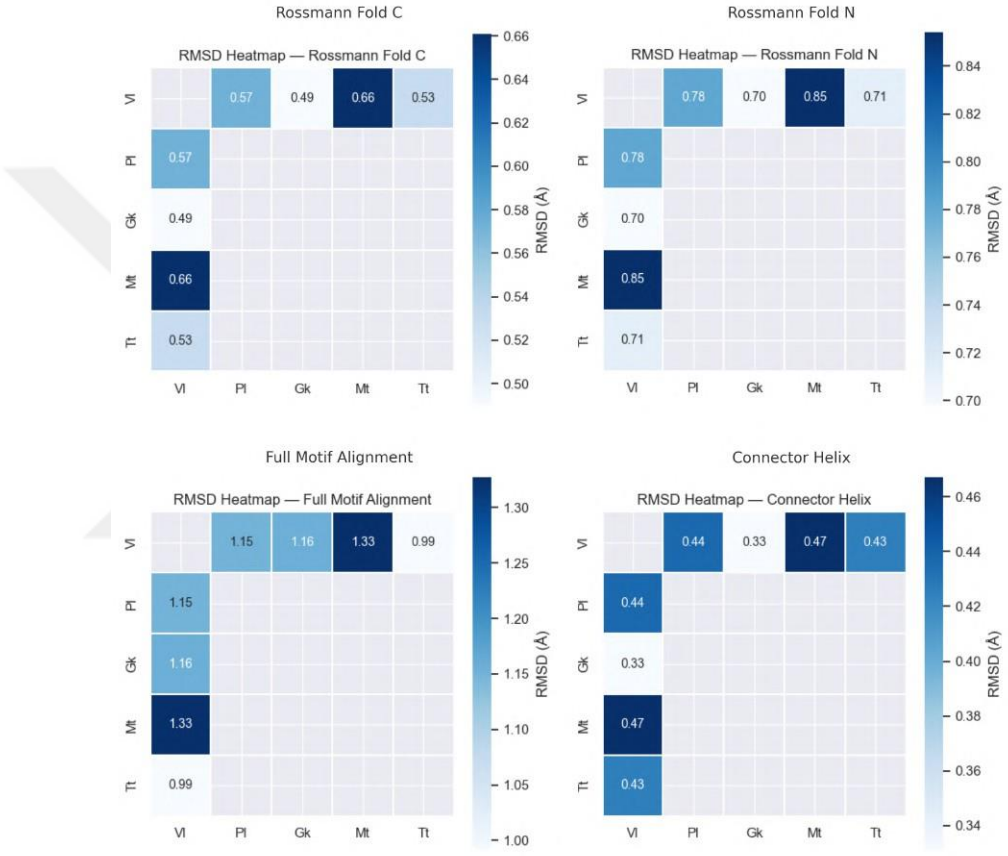

Figure 3.9: Heatmap generated based on the conserved motifs using *Vl*AlaDH as template between homolog AlaDH. Vl stands for *Vagococcus lutrae*, Pl stands for *Phormidium lapideum*, Gk for *Gebacillus kaustophilus*, Mt for *Mycobacterium tuberculosis* and Tt for *Thermus thermophilus*. Title Rossmann Fold C describes C-terminal Rossmann Fold and Rossmann Fold N describes N-terminal Rossmann Fold.

Structural alignments were and shown visually (Figure 3.10, 3.11, 3.12, 3.14), performed based on the protein backbone conservation of *Vl*AlaDH with its homologs in their apo forms, *Pl*AlaDH (PDB ID: 1PJB) and *Mt*AlaDH (PDB ID: 2VHY).

The structural alignment of the connector helix region (Figure 3.10) (residues 129–149 for *Vl*AlaDH and *Pl*AlaDH; 125–147 for *Mt*AlaDH) gave RMSD values of 0.435 Å for *Vl*AlaDH compared to *Pl*AlaDH, and 0.467 Å for *Vl*AlaDH compared to *Mt*AlaDH, therefore indicating very little structural differences. Essential for the position and stabilization of the NAD^+ molecule, the connector helix is structurally conserved among the homologs.

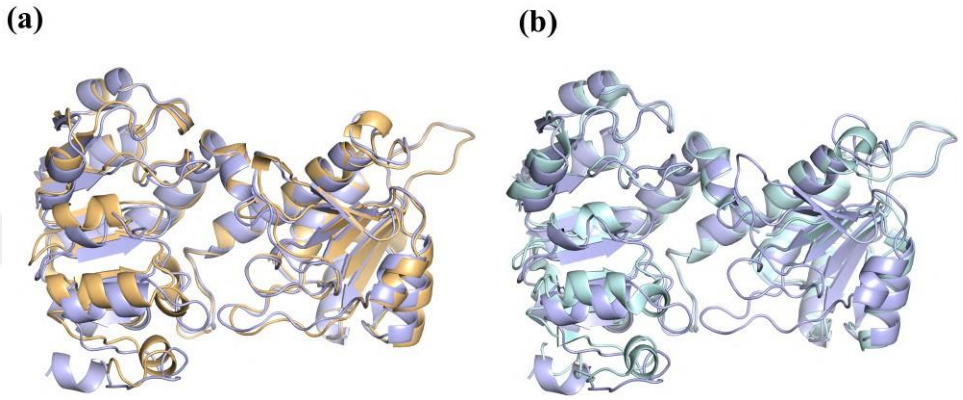

Figure 3.10: Structural alignment of the connector helix region of *Vl*AlaDH (residues 129–149), (a) *Pl*AlaDH (residues 129–149), and (b) *Mt*AlaDH (residues 125–147). *Pl*AlaDH is colored light orange, *Mt*AlaDH is colored pale cyan and *Vl*AlaDH is colored light blue.

RMSD values of 0.774 Å for *Vl*AlaDH relative to *Pl*AlaDH and 0.854 Å (Figure 3.11) for *Vl*AlaDH were obtained by means of the structural alignment of the N-terminal Rossmann fold region (residues 1–128 and 297–371). The catalytic area of an enzyme is its N-terminal Rossmann fold; the observed structural conservation suggests the maintenance of catalytic activity across species.

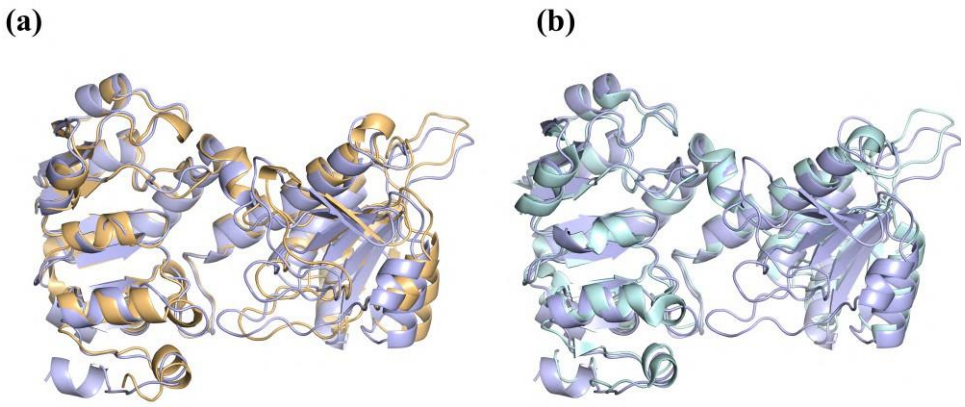

Figure 3.11: Structural alignment of the N-terminal Rossmann fold region of *Vl*AlaDH (residues 1–128 and 297–371), *Pl*AlaDH (residues 1–128 and 301–361), and *Mt*AlaDH (residues 1–124 and 301–377). *Pl*AlaDH is colored light orange, *Mt*AlaDH is colored pale cyan and *Vl*AlaDH is colored light blue.

The structural alignment of the C-terminal Rossmann fold region (Figure 3.12) (residues 149–300 for *Vl*AlaDH) yielded RMSD values of 0.598 Å for *Vl*AlaDH compared to *Pl*AlaDH, and 0.649 Å for *Vl*AlaDH compared to *Mt*AlaDH. The C-terminal Rossmann fold provides essential residues for NAD^+ binding, and the structural integrity suggests a conserved design for NAD^+ binding.

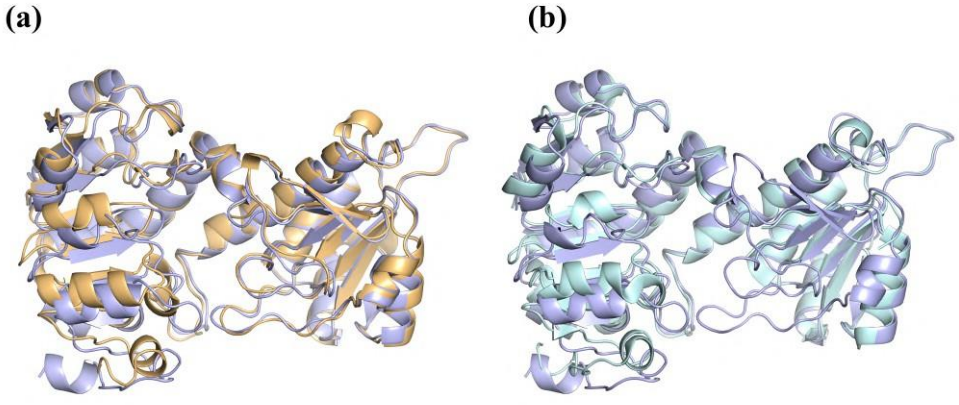

Figure 3.12: Structural alignment of the C-terminal Rossmann fold region of *Vl*AlaDH (residues 149–300), PlAlaDH (a) (residues 150–300), and *Mt*AlaDH (b) (residues 148–300).*Pl*AlaDH is colored light orange, *Mt*AlaDH is colored pale cyan and *Vl*AlaDH is colored light blue.

The integrated alignment of the N-terminal Rossmann fold, connector helix, and C-terminal Rossmann fold regions produced RMSD values of (a)1.165 Å for *Vl*AlaDH compared to *Pl*AlaDH, and (b) 0.797 Å for *Vl*AlaDH compared to *Mt*AlaDH. The conservation of these structural motifs reinforces the maintenance of the canonical L-alanine dehydrogenase fold.

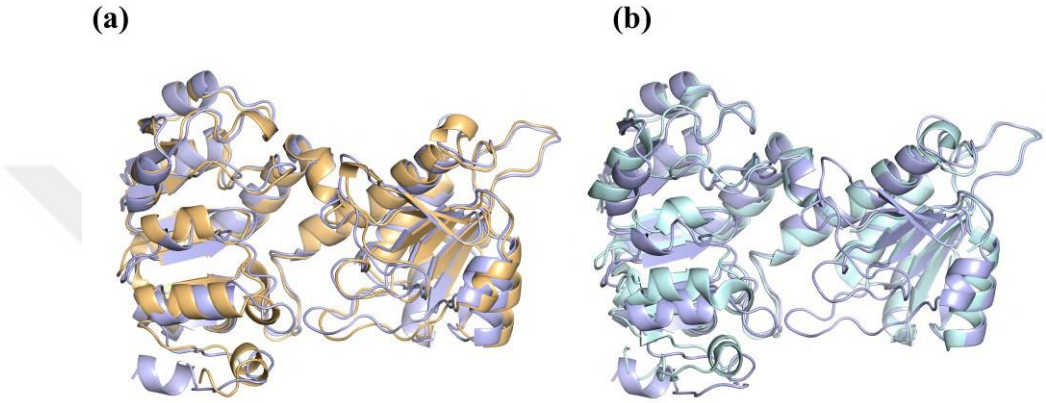

Figure 3.13: Structural alignment of *Vl*AlaDH (residues 1–128, 129–149, 149–300, and 297–371), *Pl*AlaDH (a) (residues 1–128, 129–149, 150–300, and 301–361), and *Mt*AlaDH (b) (residues 1–124, 125–147, 148–300, and 301–377), based on the combined Rossmann folds and connector helix. *Pl*AlaDH is colored light orange, *Mt*AlaDH is colored pale cyan and *Vl*AlaDH is colored light blue.

3.3.4 Phylogenetic Context of AlaDH Homologs

To see the *Vagococcus lutrae* AlaDH in the evolutionary basis in relation with other homologs, a phylogenetic tree was constructed using multiple sequence alignment of 13 representative bacterial AlaDH sequences. *Vl*AlaDH forms a separate branch, separate from well-characterized thermophilic homologs such as *Tt*AlaDH and *Gk*AlaDH (Figure 3.14).

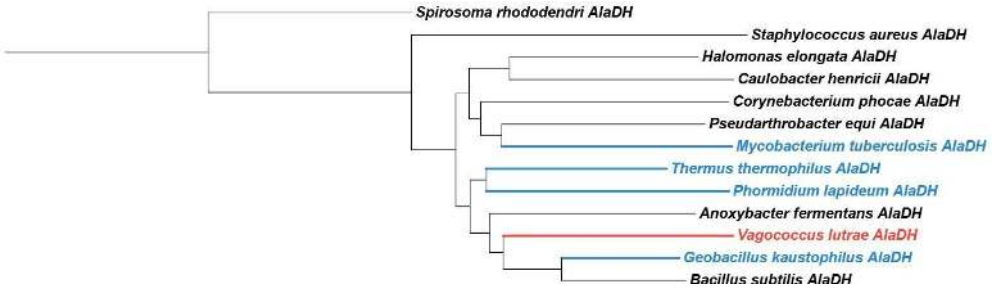

Figure 3.14: The tree constructed based on multiple sequence alignment using 13 distinct bacteria species and rooted using *Spirosoma rhododendri* AlaDH as an outgroup. *Vl*AlaDH is highlighted in red. Blue branches indicate AlaDH proteins with available crystal structures.

This phylogenetic tree clustering supports the selection of representative homologs to be used for further detailed analysis in the sequence and structure level. To further analyze the functional conservation in the selected homologs' active site and allosteric site have been compared structurally and sequentially.

3.3.5 Comparison of Active and Allosteric sites with Homolog AlaDH Structure

The active site of *Vl*AlaDH was analyzed in relation to homologous AlaDH structures from *Phormidium lapideum* (PDB ID: 1SAY) and *Mycobacterium tuberculosis* (PDB ID: 2VHY) to examine the conservation of substrate recognition and catalytic characteristics. Structural alignment indicated that critical residues associated with pyruvate binding—Arg15, Lys74, Tyr94, His95, and Met132—are conserved in both spatial and functional aspects across all analyzed structures (Figure 3.15).

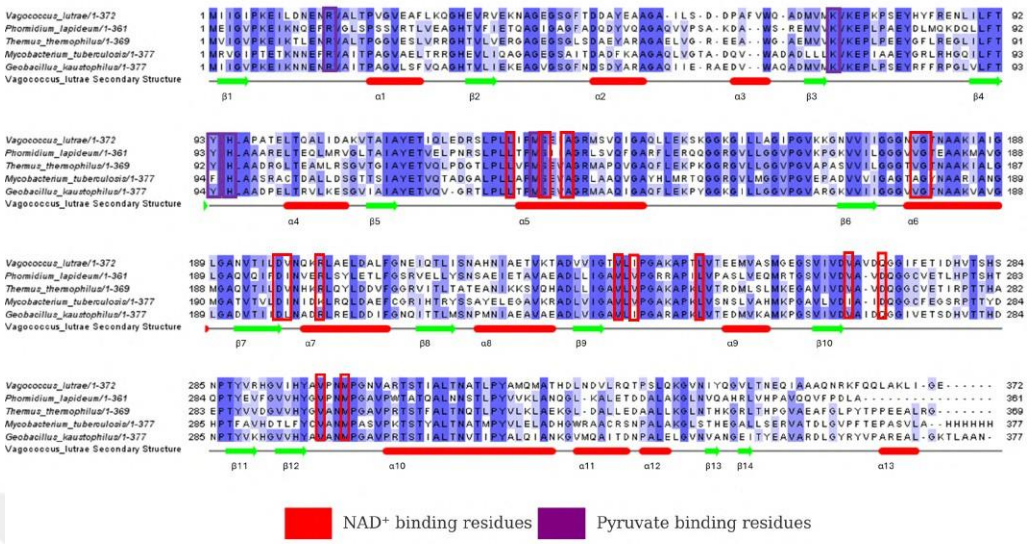

Figure 3.15: Multiple sequence alignment of VlAlaDH with homologous alanine dehydrogenases from *Phormidium lapideum*, *Mycobacterium tuberculosis*, *Geobacillus kaustophilus* and *Thermus thermophilus*. Highly conserved residues are shaded in blue. Secondary structure elements of *Vl*AlaDH are shown below the alignment.

To visualize the spatial relation of the substrate and the cofactor, pyruvate and NAD respectively, the ligands were modeled into the sites based on the homolog alignment (Figure 3.15). The aligned pyruvate extracted from *Phormidium lapideum AlaDH* (*Pl*AlaDH) (PDB ID: 1SAY), and the NAD+ is from *Mycobacterium tuberculosis* AlaDH (*Mt*AlaDH) (PDB ID: 2VHX). The proximity of the nicotinamide ring of NAD^+ to pyruvate reflects the catalytic arrangement seen in homologous AlaDH enzymes.

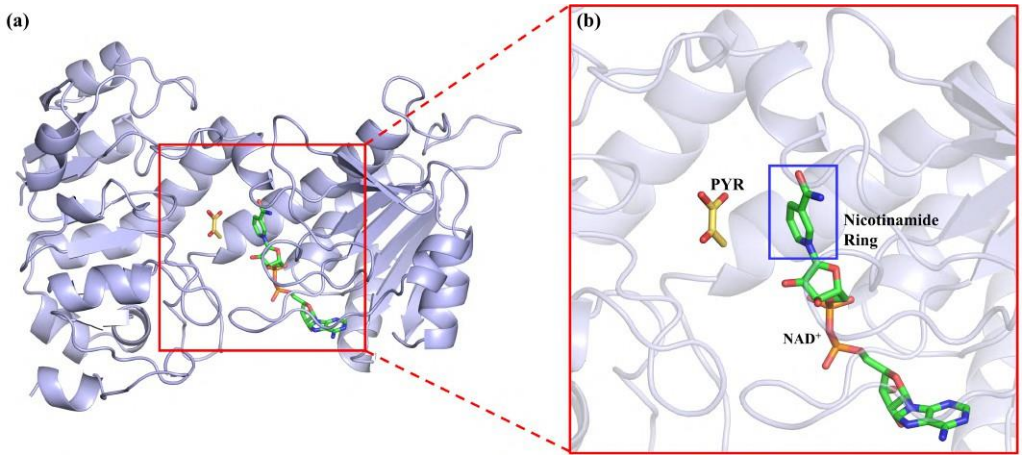

Figure 3.16: (a) Zoomed out view of the VlAlaDH monomer in cartoon representation (light blue) with superposed pyruvate (yellow) and NAD (green), modeled from homologous structures. (b) Zoomed-in view of the active site showing pyruvate adjacent to the nicotinamide ring of NAD^+

Figure 3.17 illustrates that these residues participate in stabilizing interactions with the ligand, where Arg15, Lys74, and His95 each establish direct hydrogen bonds with pyruvate and Tyr94 and Met132 contacted by hydrophobic interactions. The contacts are crucial for orienting the substrate within the catalytic cleft and are preserved with high fidelity across homologs.

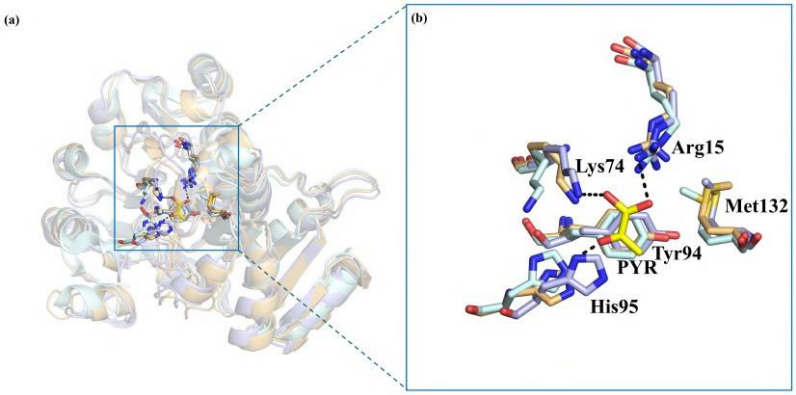

Figure 3.17: Structural alignment of *Vl*AlaDH (light blue), PlAlaDH (light orange), and MtAlaDH (pale cyan) highlighting the spatial arrangement of the active site cleft. (a) Overall view showing the location of the catalytic pocket. (b) Zoomed-in view of the aligned active sites, illustrating conserved residues involved in pyruvate binding. Possible hydrogen bonds shown as black dashed lines.

To visualize the possible NAD^+ binding cleft in the discovered *Vl*AlaDH structure, the NAD^+ from homologous *Mycobacterium tuberculosis* AlaDH (PDB ID: 2VHX) has been super imposed onto the apo *Vl*AlaDH structure (Figure 3.18). The interacting residues surrounding the cofactor were identified based on the *Geobacillus kaustophilus* (PDB ID: 8HYH). Both 2VHX and 8HYH structures consist of 377 residues, closely matching the 372 residues of *Vl*AlaDH. This high similarity allowed reliable superposition of NAD^+ coordinates from 2VHX, while using 8HYH to define conserved binding residues.

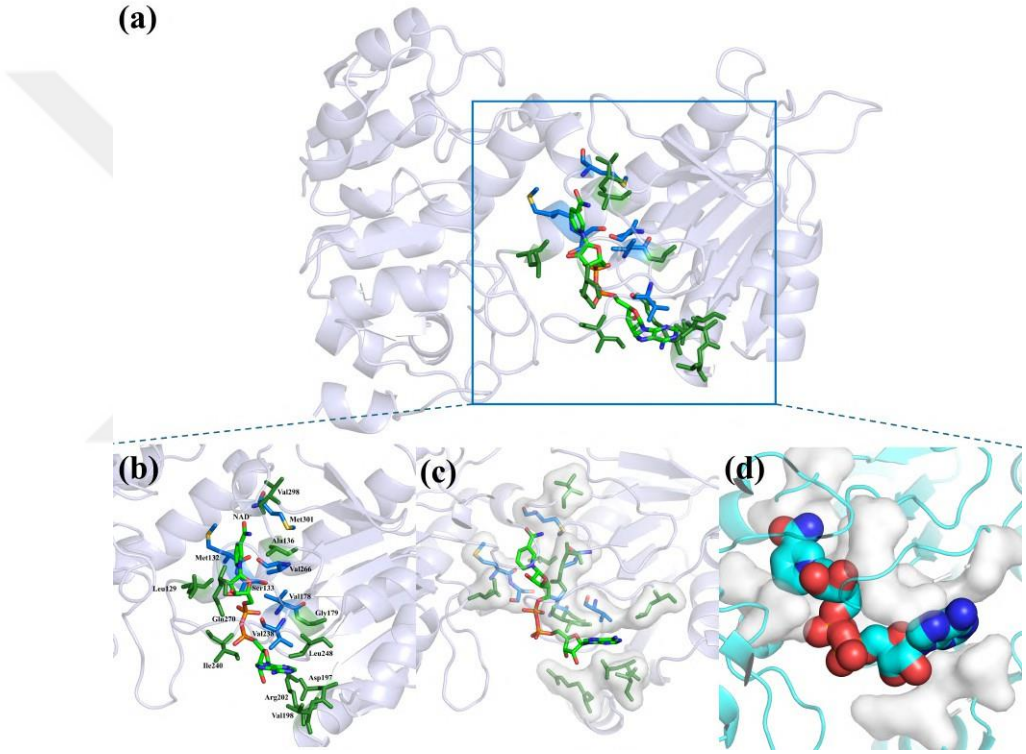

Figure 3.18: Structural visualization of the predicted NAD binding site in *Vagococcus lutrae* alanine dehydrogenase (*Vl*AlaDH) via homolog alignment. Panel (a) shows a cartoon representation of the *Vl*AlaDH monomer with NAD^+ positioned in the interdomain cleft based on homolog superposition. Panel (b) presents a zoomed-in view of the predicted binding pocket with labeled interacting residues. Panel (c) displays the surface rendering of the binding site, highlighting the pocket's shape and accessibility. Panel (d) shows the space-filling model of NAD^+, demonstrating steric complementarity within the binding cleft. The residues with hydrogen bonding ability have been colored blue, the ones interact hydrophobically are colored green.

Comparing the first done with the NAD^+ binding cleft was done using the conserved NAD^+ binding motif. The conserved residue is the part of the N-terminal Rossmann fold

region where it has been kept intact among the species. The motif sequence goes GxGxxG where the x is signified as the variable residue (Lensk,1995). The described region (Figure 3.19) orients the pyrophosphate moiety of the NAD^+.

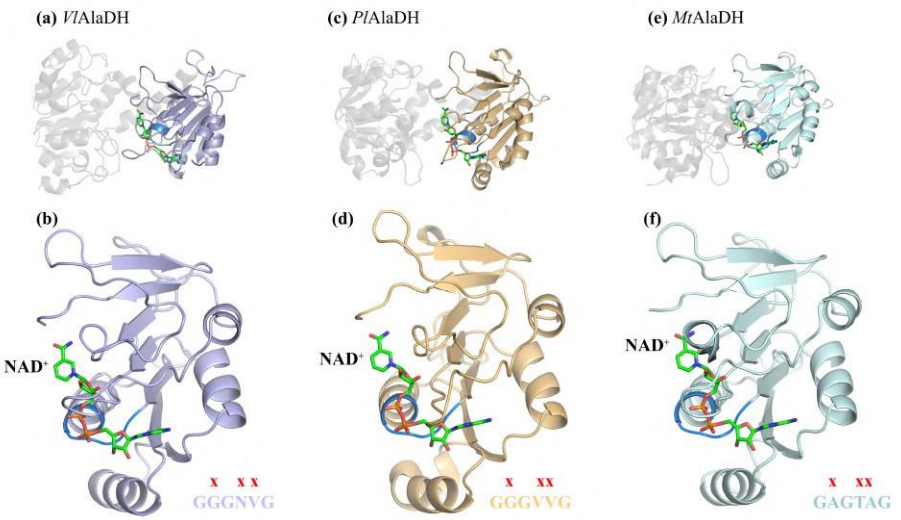

Figure 3.19: (a-b) *Vagococcus lutrae* AlaDH (*Vl*AlaDH) and focused on view of the binding motif (c-d) *Phormidium lapideum* AlaDH and focused on view of the binding motif (*Pl*AlaDH, PDB: 1PJB), and (e-f) *Mycobacterium tuberculosis* AlaDH and focused on view of the binding motif (*Mt*AlaDH, PDB: 2VHX) structures highlight the glycine-rich Rossmann fold motif involved in NAD^+ binding. The canonical GxGxxG motif is shown beneath each structure, and conserved residues are displayed in stick representation near the NAD^+ binding cleft. Colors correspond to motif-matching cartoon colors in each panel. The variable residues in the motif colored as red on top of the motif sequence.

Structural and sequence-level conservation within the NAD^+-binding region was assessed through the analysis of surface representations and multiple sequence alignments for *Vl*AlaDH, *Pl*AlaDH, and *Mt*AlaDH. Structural representations of the cleft from both frontal and rotated perspectives indicate that the NAD^+-binding pocket's overall shape is maintained across homologs, thereby reinforcing a shared binding topology (Figure 3.20). NAD^+ was either modeled or superimposed by *Mt*AlaDH to assess its compatibility within the cleft. The alignment of residues 129–300, encompassing the Rossmann fold, demonstrates significant conservation at critical positions, especially in motifs linked to NAD^+ anchoring. Color coding according to residue identity highlights conserved regions that likely play a role in cofactor recognition and structural stability.

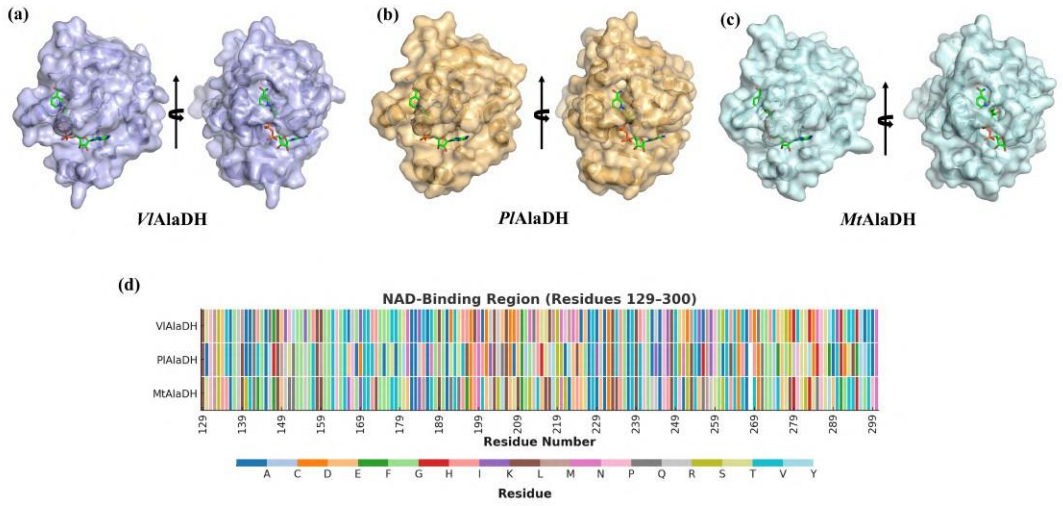

Figure 3.20: (a–c) Surface representations of *Vl*AlaDH (a), *Pl*AlaDH (b), and *Mt*AlaDH (c) in complex with NAD, shown in two orientations rotated 90° along the vertical axis. NAD^+ molecules are displayed in stick representation to highlight their position within the binding cleft. (d) Heatmap representation of the multiple sequence alignment for residues 129–300, corresponding to the NAD^+-binding region. Rows correspond to the three homologs, and each residue is color-coded based on amino acid identity. The color key below the alignment panel indicates residue types.

Surface potential maps were generated to assess the electrostatic compatibility of the NAD^+ binding cleft among homologs, specifically *V. lutrae* AlaDH (*Vl*AlaDH), *P. lapideum* AlaDH (*Pl*AlaDH), and *M. tuberculosis* AlaDH (*Mt*AlaDH). All three structures displayed a distinct electropositive region (blue) encircling the pyrophosphate- and nicotinamide-binding pockets.

The features were particularly concentrated in the cleft created by conserved motifs of the Rossmann fold. Due to the lack of native NAD^+ coordinates for *Vl*AlaDH and *Pl*AlaDH, the cofactor was superimposed using the holo MtAlaDH structure (PDB ID: 2VHX) (Figure 3.21). The analogous electrostatic environment present in the homologous clefts reinforces the structural validity of this superposition. The 90° Y-axis rotated views indicate that the positively charged pocket extends significantly into the cofactor-binding groove, highlighting the electrostatic complementarity necessary for NAD^+ stabilization and uniform cofactor positioning among AlaDH homologs.

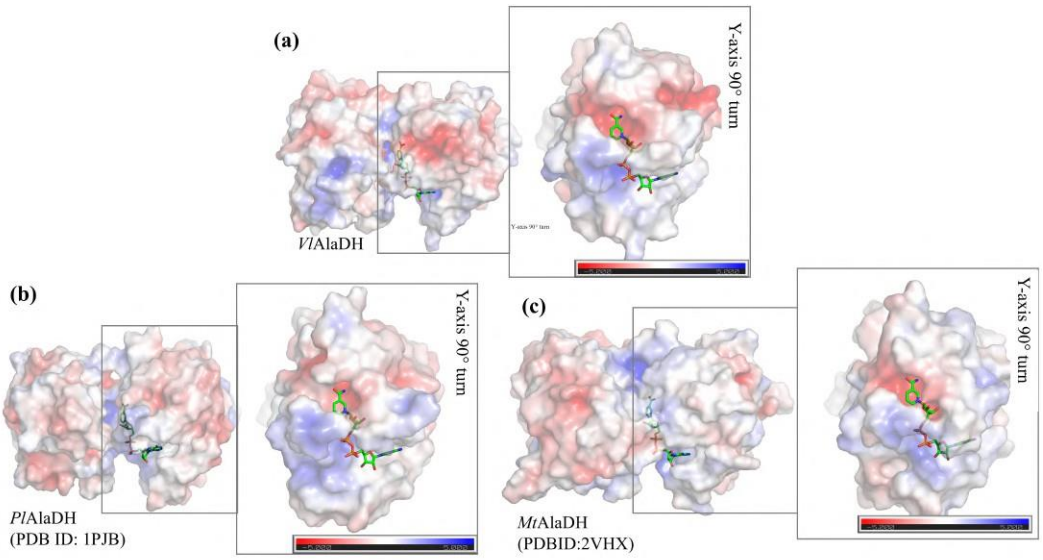

Figure 3.21: Electrostatic surface representations of the NAD^+ binding clefts in *Vagococcus lutrae* AlaDH (this study), *Phormidium lapideum* AlaDH (PDB ID: 1PJB), and *Mycobacterium tuberculosis* AlaDH (PDB ID: 2VHX) are presented. Both front and 90° Y-axis rotated views are presented for each structure. Surface potentials were computed utilizing APBS and are represented with a color gradient from 5.0 (red) to +5.0 (blue). NAD^+ is depicted in stick representation and was superimposed onto *Vl*AlaDH and *Pl*AlaDH according to alignment with the holo *Mt*AlaDH structure.

3.4 Ligand Binding and Docking Studies

Molecular docking was conducted using CB-Dock2 (Liu et al., 2022; Yang et al., 2022) to examine the substrate-binding properties of *Vl*AlaDH with pyruvate, various α-keto acid analogs, and L-alanine. All ligands consistently docked in the same primary cavity, which corresponds to the predicted active site of the enzyme (Figure 3.22). The conserved binding site corresponds with the experimentally characterized catalytic cleft, indicating precise pose prediction by the docking algorithm. The initial analysis examines the spatial localization of each ligand within the active site, emphasizing their proximity to catalytically relevant residues. The spatial overlap among substrates establishes a basis for assessing specific interactions and potential determinants of substrate specificity in the following sections.

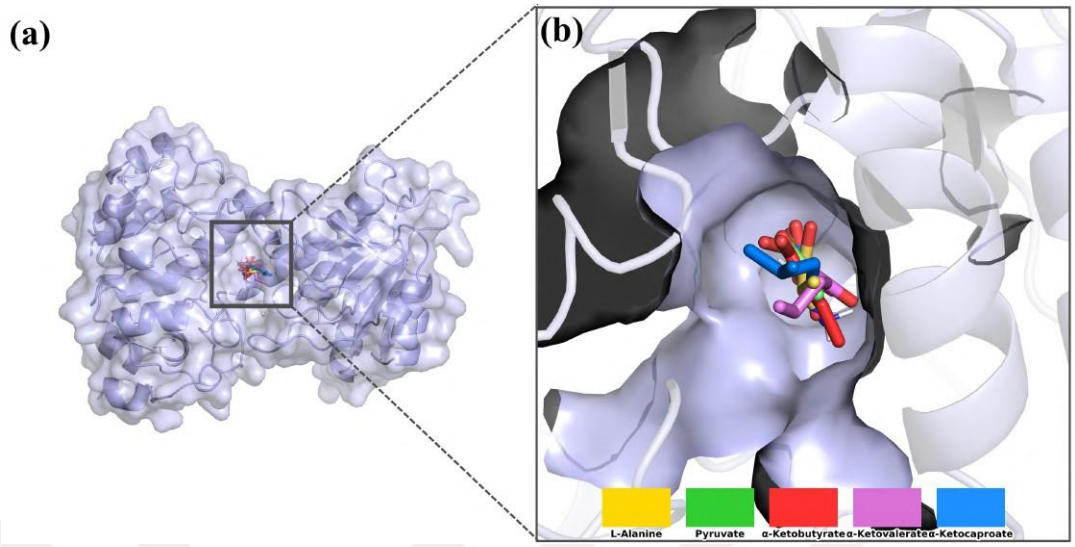

Figure 3.22: Structural visualization of the ligand-binding pocket of *Vl*AlaDH highlighting the superposed positions of five docked ligands. (a) Surface representation of the full *Vl*AlaDH monomer with bound ligands, shown in cartoon and transparent surface (light blue), with the active site region boxed. (b) Zoomed-in view of the ligand-binding cleft showing the superposed docked conformations of L-Alanine (yellow), pyruvate (green), α-ketobutyrate (red), α-ketovalerate (magenta), and α-ketocaproate (blue). The surrounding pocket residues are rendered in light blue cartoon representation. Ligand coloring corresponds to the legend displayed at the bottom of the panel.

Blind docking of five ligands—L-alanine, pyruvate, -ketobutyrate, -ketovalerate, and -ketocaproate—was conducted utilizing CB-Dock2, which integrates geometry-based cavity prediction with AutoDock Vina scoring and homologous pocket fitting (Liu et al., 2022; Yang et al., 2022). The highest-ranked cavity for all ligands aligned with the enzyme's catalytic cleft and corresponded to the substrate-binding site of *Phormidium lapideum* L-alanine dehydrogenase (PDB ID: 1SAY) (Figure 3.23).

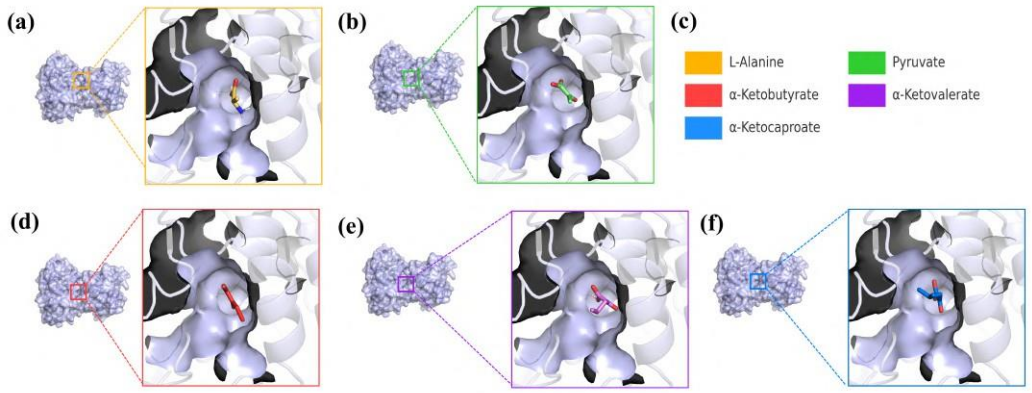

Figure 3.23: Binding poses of L-alanine, pyruvate, α-ketobutyrate, α-ketovalerate, and α-ketocaproate were obtained through blind docking into *Vagococcus lutrae* AlaDH. The panels (a-d) presents the overall surface representation of each ligand along with the bound ligand and the binding pocket seen from far. Panel c is the color map showing the color of each ligand. Docking was conducted utilizing CB-Dock2, employing pocket fitting through structural alignment. Ligands are depicted in stick representation.

The identified pocket exhibited a pocket identity of 1.0 and a pocket RMSD of 0.68 Å across all docking scenarios, indicating structural conservation. FP2 scores demonstrated that pyruvate aligned precisely with the template pocket (FP2 = 1.0), whereas -ketobutyrate exhibited moderate similarity (FP2 = 0.79). Other ligands, including alanine, α-ketovalerate, and α-ketocaproate, exhibited FP2 values approximately equal to 0.6, indicating variability in interaction patterns.

The FitDock scores, derived from AutoDock Vina predicted binding affinities, were as follows: pyruvate and alanine (2.9 kcal/mol), α-ketobutyrate (2.1 kcal/mol), α-ketovalerate (3.3 kcal/mol), and α-ketocaproate (3.4 kcal/mol). The results demonstrate similar binding energies for both the natural substrate and product, whereas larger keto acids exhibited marginally more favorable predicted affinities, presumably attributable to enhanced hydrophobic interactions.

The docking results were further analysis on possible binding interactions between the ligands and the relevant keto acids. These interactions are graphed using LigPlot+(Laskowski & Swindells, 2011) (Figure 3.24). L-alanine did not establish any hydrogen bonds with the residues found in the pocket. Pyruvate and two other keto-acids did establish hydrogen bonds with Arg15 and Lys74. α-ketocaproate did only with Lys74.

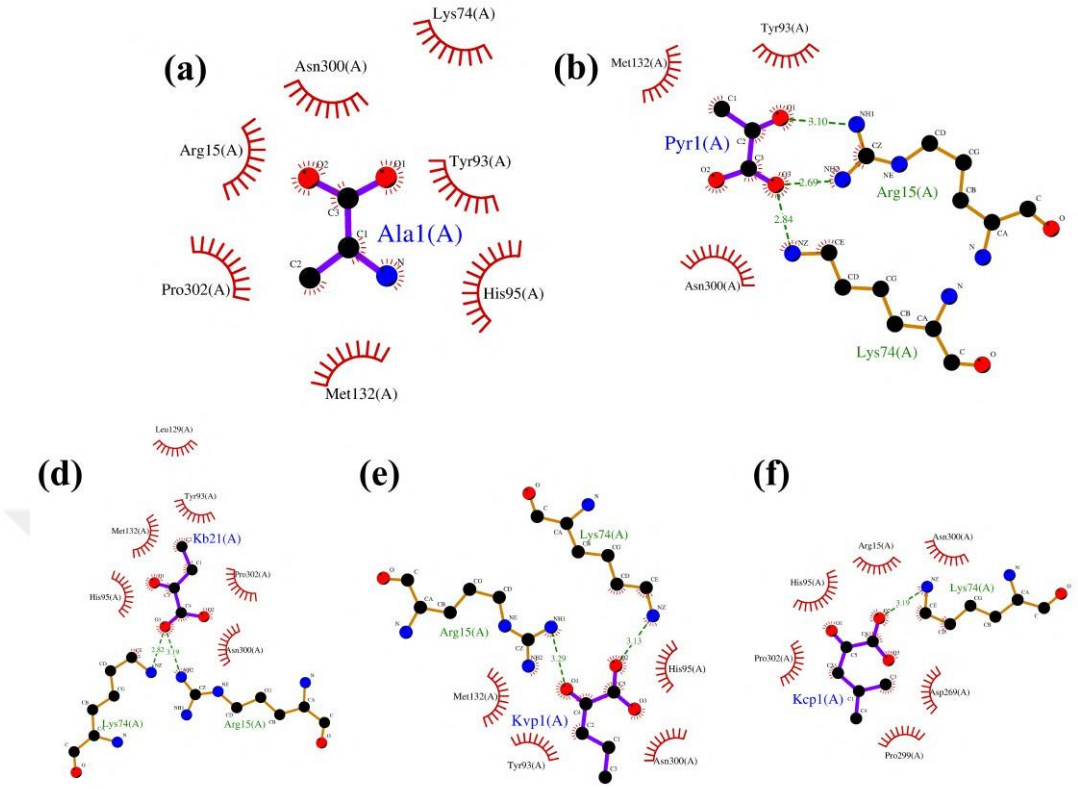

Figure 3.24: Two-dimensional ligand interaction diagrams for (a) L-alanine (Ala1(A)), (b) pyruvate (Pyr1(A)), (c) α–ketobutyrate (Kb21(A)), (d) α–ketovalerate (Kvp1(A)), and (e) α–ketocaproate (Kcp1(A)) within the proposed active site of *Vagococcus lutrae* AlaDH, derived from docking results. Hydrogen bonds are represented by green dashed lines, while hydrophobic interactions are denoted by red semicircles. Ligands are designated and color-coded appropriately. Residues that contribute to ligand stabilization are labeled with their respective chain identifiers.

Chapter 4

DISCUSSION AND CONCLUSION

The architecture revealed by apo ambient *Vl*AlaDH structure showed conserved Rossmann fold, with these being in N-terminal and C-terminal connected by a helical segment called as connector helix. Structural alignment was based on these motifs with homologs from *Phormidium lapideum* and *Mycobacterium tuberculosis*. Mycobacterium tuberculosis, being a human pathogen, adapted to survive in the average human temperature, which is 37° C, reflects mesophilic characteristic (Gray et al., 2014). On the contrast, *Phormidium lapideu*m found to be living in hot springs and geothermal setting, classified as thermotolerant cyanobacterium having some structural architecture that are adapted to higher temperatures (Wakayama et al., 1998). These two demonstrated high conservation by having under 1 Å across the motifs that were used for the alignment. The main difference between the structures were in the Rossmann fold motifs where the loops varied among homologs. Among these, *Vl*AlaDH showed closer structural similarity to *Pl*AlaDH than to *Mt*AlaDH. Even though the difference between the homologs with different thermal tolerance, the core structure is shared among divergent species

Using PISA analysis, assembly was confirmed that *Vl*AlaDH forms a stable hexameric assembly. This result has been based on the values first with the buried surface area (BSA) having approximately 18,000 $Å^2$, which far exceeds the commonly agreed upon threshold value of 2,000 $Å^2$ per interface for biologically relevant assemblies (Krissinel & Henrick, 2007). Further proof comes from the free energy change signified by ΔG_{int}, interaction free energy where shows the energy gained with the two or more protein interact, and Gdiss, dissociation free energy where it shows the energy required to breaking the formed oligomer. First, ΔG_{int} for the possible hexameric assembly gave the value of -79.4 kcal/mol signifying strong and favorable formation. Second, ΔG_{diss} value given to the possible hexameric assembly is 8 kcal/mol suggesting its not easily dissociates in the solution (Krissinel & Henrick, 2007). An alternative oligomerization of dimerization

showed a higher ΔG_{diss} of 14.9 kcal/mol with higher value ΔG_{int} of -19.2 kcal/mol. The oligomerization trend indicates that *Vl*AlaDH predominantly exists as a hexamer, which dissociates into three dimers, with no additional breakdown beyond this state.

For further evaluation of the biological assembly, the space group H 3 2 supports the assembly by its threefold rotational symmetry. Even though the MR pipeline and further refinement didn't result in hexameric structure, the hexameric assembly could be generated using symmetry operations with the tools such as PISA used in this research. This discrepancy happens in crystallography when combining the crystallographic assembly and biological assembly.

The possibility of hexameric assembly is further analyzed with Matthew's coefficient where it is based on the following formula:

$$V_m = \frac{V_{cell}}{N \cdot M} \tag{4.1}$$

where V_{cell} is the unit cell volume in Å^3, N is the number of proteins per unit cell, and M is the molecular weight of monomer in Da. The calculated unit cell volume was approximately 2.30 × 10 Å^3, and the molecular weight shown in the SDS-Page gel is 39.7 kDa. When given the protein content per unit cell as one monomer, the resulting Matthew's coefficient (V_m) was calculated as 59.7 Å^3/Da which makes the solvent content as 97.9%. The resulting (V_m) value does not fall in between acceptable range of 1.7 and 3.5 Å^3/Da, with solvent content again falling in between 30% to 70% (Matthews, 1968; Kantardjieff & Rupp, 2003). To achieve the result in between the acceptable range, the number of proteins per unit cell would be changed into 18 monomers, making it three biological hexamers, decreasing the coefficient to 3.22 Å^3/Da. The solvent content therefore sat in the acceptable range with the value of approximately 61.7%. The findings provide solid proof for the existence of three hexamers per unit cell, thereby reinforcing the conclusion that the hexameric assembly identified in *Vl*AlaDH holds biological significance.

Similar arrangements in the crystal structure of *Phormidium lapideum* AlaDH (PDB ID: 1PJB) could be seen as it also crystallized in the same space group of H 3 2 with asymmetric unit carrying one monomer. The lack of oligomeric asymmetric unit does not disobey since the assembly predicted crystallographic symmetry using PISA. This

structural similarity based on the crystallographic symmetry reinforces the idea that the hexameric assembly is conserved and biologically significant feature shared among the AlaDH homologs.

The model generated using AlphaFold from AlphaFold Protein Structure Database, to be used as initial search model in the experimental pipeline for MR in Phenix where it provided the phase information. The model showed a high per-residue confidence score which signified as pLDDT which is generally above 90. The labeled as confident residues are included throughout the N-terminal Rossmann fold, C-terminal Rossmann fold and connector helix linking two domains. Only part of the prediction had slightly less confidence of pLDDT between 70 and 90 was a part of a long loop between a flanking helices and beta strand. The model used for the MR process without trimming or pruning of the model.

Structural comparison of the N-terminal Rossmann fold, C-terminal Rossmann fold, and connector helix revealed strong agreement with the experimentally solved structure. The RMSD values for comparing the motifs showed a trend of less than 1 Å which means that they are close structurally. The C-terminal alignment gave the smallest RMSD value of 0.386 Å where the crucial cofactor NAD^+/NADH binds. The deviations are again like homolog structures are limited to flexible loop regions. Even though multimeric predicted was available in the database, no multimeric comparison was made in this study. By using only the monomeric prediction, the model helped to solve the biologically relevant hexameric structure where AlphaFold might not be able to predict with no experimental data backing it up.

The NAD^+ binding site is found in the C-terminal Rossmann fold which follows the main function of the super secondary structure. Here we first have shown the probable NAD^+ cleft based on homolog structural alignment. The NAD^+ originally bound to homolog *Mycobacterium tuberculosis* have been superimposed to the apo *Vl*AlaDH where it was confirmed by the other homologs to be the correct location. Also, we have shown the surfaces of the residues surrounding the NAD^+ which was based on another homolog structure Geobacillus kaustophilus to establish the space fill representation of NAD^+. The space fill representation also proved the location of the cleft by fitting in the cleft formed in the way that predicted.

Comparing the residues interacting have been mostly conserved. The first outlier being Val198 where it is only shared with the homolog from *Thermus thermophilus*, other homologs *Mycobacterium tuberculosis* and *Phormidium lapideum* residue number 198 carries Ile. The remaining homolog *Geobacillus kaustophilus* has Leu in that location. These residues belong to the non-polar type and the average size of the residues being similar, these substitutions would not differentiate the general behavior of the interaction. The valine substituted in *Vl*AlaDH forms hydrophobic interaction like other residues in that location being in close contact with both adenine ribose and β-phosphate of NAD^+ making it an effective residue that contributes to the cleft's contour and cofactor stabilization.

Another outlier out of NAD^+ binding residues from *Vl*AlaDH is Ile240 that is also shared with *Geobacillus kaustophilus*. The three other homologs carry the same residue in that location which is Val. This residue near the nicotinamide end of NAD^+ is likely carrying out Van der Walls interaction between the nicotinamide end, while helping to fix in the end to effectively process the redox reaction between the pyruvate and NAD^+ . Sharing this residue with *Geobacillus kaustophilu*s may be beneficial evolutionarily for NAD^+ fix better than the other homologs since *Geobacillus kaustophilus* is a type species that is adapted to surviving generally high temperatures (Zhou et al., 2019). Being bulkier than valine might be more effective in orienting the NAD^+ and supporting optimal alignment for catalysis.

At the location of residue 270, two residues are prevalent. For *Vl*AlaDH and *Gk*AlaDH this residue is Gln270, the remaining homologs in the MSA have Asp270 in that location. This location is found near NAD^+ likely interacting with hydrogen bonds. Replacing aspartate to glutamate results in the removal of negative charge at that location replacing it with a polar but uncharged residue that still retains hydrogen bonding capability with its side chain. This shift in sequential level might alter the electrostatic behavior of the binding cleft and influence how NAD^+ is stabilized. Since aspartate is more prevalent at this position, the presence of glutamine in *Vl*AlaDH may reflect a species-specific adaptation possibly affecting the binding behavior of NAD^+ in both dynamics and flexibility.

Although a ligand-bound structure is not available in the current scope of this study, the location of the residue the close proximity to the cofactor makes it a plausible candidate for further investigation.

Detailing the comparison in residue level, the critical NAD^+ binding motif located in the Rossmann fold with the sequence of Gx_1Gx_2x_3G preserves the glycine rich core across homologs, but the residues represented by "x" vary. While the conserved glycines provide the necessary flexibility for the pyrophosphate moiety to which the motif is in close proximity to, the side chain differences at "x" positions may influence the NAD^+ binding through changes in shape, dynamics, and or at the local environment. In *Vl*AlaDH, the motif aligns well within those other homologs though small differences are present due to species-specific adaptations.

In *Vl*AlaDH the residues in x_1 and x_3 of G$x_1$1Gx_2x_3G are shared with *Pl*AlaDH whereas Mycobacterium tuberculosis differs at all three 'x' positions. The x_2 shows the highest variable across these three homologs. These include Asn (N) in the *Vl*AlaDH, Val(V) in the *Pl*AlaDH, and Thr(T) in *Mt*AlaDH. Asparagine, found in *Vl*AlaDH, provides strong hydrogen bonding potential stronger hydrogen bonds than Thr at that location where the pyrophosphate moiety of NAD^+ is the interaction partner. Valine, present in *Pl*AlaDH, lacks the ability of hydrogen bounding capacity, but the residue might reflect the preference of hydrophobicity due to adaptability of the nonpolar enzymes in the thermostable organisms like *Phormidium lapideum*.

The overall shape of this NAD^+ binding cleft across the homologs including *Vl*AlaDH has been conserved. Despite the minimal variations, such as slight narrowing of the cleft *Mt*AlaDH, the cleft stays generally open and accessible in the structures in all compared structures. The cleft is not a completely closed pocket, making the volume calculation was not possible in the desired way. To extend our comparison from the surface level, a residue heatmap was generated. The resulting heatmap showed limited conservation in the region except the residues that directly interact with the NAD^+. Most residues encompassing the main interaction site varied between species, indicating of the structural plasticity. Even with these differences the overall Rossmann fold architecture is maintained that supports NAD incorporation into the 3D cleft. The main interacting residues are conserved, the surrounding solvent exposed regions of the enzyme show more hydrophilic characteristic.

Characteristics are done thoroughly focusing on the cofactor binding cleft. Discussion will continue with the active site with catalytic residues and recognizing residues, in particular ones that are responsible for pyruvate binding and the enzymatic redox reaction.

Critical residues in close contact with the pyruvate are Arg15, Lys74, Tyr94, His95 and Met132. These residues are conserved across structurally characterized AlaDH homologs. Structural alignment based on *Pl*AlaDH and *Mt*AlaDH, revealed a highly similar spatial alignment with only minor residue shifts varying -1 and +1 in residue number. This consistent positioning forms a conserved catalytic domain across structures analyzed in the scope of this study. The conservation of these residues was further confirmed through the MSA, which included all the AlaDH with crystal structures. Although pyruvate is a simple three-carbon molecule but crucial in the metabolism of the organism, the strict conservation of interacting residues underlines the importance of this active site architecture for its functional importance and evolutionary stability involved in pyruvate recognition and redox catalysis.

Molecular docking studies were performed using pyruvate, L-alanine and a set of related keto acid to assess potential substrate interactions with the active site. In addition, by docking pyruvate-related keto acids were used to explore potential alternative substrates that could offer advantages over pyruvate. The result established as Arg15 and Lys74 the primary residues pair involved with hydrogen bonding for pyruvate and two other keto acids, which are consistent roles with homologs that have been discussed in this study. The one ketoacid that didn't follow this trend was α-ketocaproate. The reason could be that since it carried longer carbon chain, it only interacted with Lys74 not anymore with Arg15. The size of the substrate affects the precise binding geometry. The missing residue that conversed among the homologs and established the foundation of hydrogen bonding network based on the homological structural comparison, His94 was absent in the docking results. The absence of the His94 in the docking results shows that this residue is not responsible for interacting and keeping it in place during the catalysis of the reaction, rather it is responsible for acid/base catalysis of the reaction, possibility needs the cofactor binding in order to move and interact with the substrate.

The L-lactate dehydrogenase (L-LDH) comparison between L-Alanine dehydrogenase done which further proves active site residues functional assignments. In both enzymes,

the stabilization of the carboxyl group of both lactate and pyruvate done via arginine residue (Arg15 in L-AlaDH; Arg169 in L-LDH), the carbonyl group is polarized by a positively charged residue (Lys74 in L-AlaDH; Arg106 in L-LDH) and a conserved histidine catalyzes acid/base catalysis (His95 in L-AlaDH; His193 in L-LDH). These parallels in the residue level and in the catalytic activity support the idea that the docking reflects such information even if the conserved residues do not appear in the docking results as well as not interact without the cofactor. The NAD^+ wasn't bound due to the technical difficulties but was able to be inferred based on homolog alignment.

A phylogenetic tree was constructed using 13 distinct species in order to see how closely related to each species' AlaDH are to each other and what this entails to our study of *Vl*AlaDH. *Vl*AlaDH clustered separately and didn't share any close root to any other species. The groups were based upon the characteristics of organisms such as thermophilic or pathogenic. These types of organisms can be named *Geobacillus kaustophilus* and *Mycobacterium tuberculosis* where *Vagococcus lutrae* appears in its distinct group being a marine based organism. Even though evolutionary they are all distinctive to each other, the enzyme AlaDH shared between these keeping the core of the protein, Rossmann fold architecture and catalytic residues, without largely changing due to the evolutionary pressure. This evolutionary insight supports the observed structural and functional similarities revealed through comparative analysis.

To conclude, this study presents the first ambient apo structure of L-Alanine dehydrogenase from *Vagococcus lutrae* (VlAlaDH) where the enzyme was characterized both structurally and computationally, expanding current knowledge of this recently identified organism and its potential future industrial applications. The crystal structure was solved at 3.2 Å resolution, featuring two conserved Rossman fold structures, consistent NAD^+ binding motifs, and quaternary assembly of hexamer as supported by PISA-based biological assembly prediction that matches what is observed in other bacterial AlaDH homologs. Structural alignments based on both major motifs and the residue level alignment of active pocket and allosteric site, across the homologs from *Mycobacterium tuberculosis*, *Phormidium lapideum*, *Geobacillus kaustophilu*s, and *Thermus thermophilus* revealed a high degree of conservation among them.

Molecular docking supported these structural findings, showing favorable binding of

the main substrates of pyruvate, L-alanine and the pyruvate related ketoacids. However, despite this success in the computational analysis, the information related to experimental binding of these ligands is missing due to the structure being in the apo form as well as the moderate resolution of 3.2 Å. Additionally, the scope of the current information on kinetic properties of the enzyme is the enzyme's kinetic parameters of K_m and K_{cat} and the optimum working pH of the enzyme. Theres no available data on features relevant to industrial applications, such as thermostability or the organism's overall metabolic flexibility. As *V.lutrae* hasn't been characterized extensively in general, there is especially no current study of its enzymatic properties. Therefore, this study marks an important steppingstone in the right direction for the enzymatic work that will follow this.

In terms of future research goals for this project, the co-crystallization of *Vl*AlaDH with its native ligands such as pyruvate, L-alanine, NAD^+ and NADH needs to be prioritized. This process needs to be done to validate the docking results as well as experimentally based comparison with the ligand bound homolog structures. Another goal would be to thermostability assay studies followed by mutagenesis studies to be done. The mutagenesis would likely target NAD^+ binding residues where it is most varied as terms of interaction with a focus of the area of NAD^+'s nicotinamide moiety where it could help reveal structural features that influence both substrate recognition and cofactor interaction. Further exploration of other possible dehydrogenases or industrially applicable in the *Vagococcus lutrae* genome may also uncover additional biocatalyst with industrial potential. The current study provides a first step in revealing this organism's wider biochemical capabilities, considering its limited enzymatic characterization.

BIBLIOGRAPHY

Altintas, I., Andrews, V., & Larsen, M. V. *(2020).* First reported human bloodstream infection with Vagococcus lutrae. New Microbes and New Infections, 34, 100649.

American Chemical Society. (2021). *L-Alanine*. ACS Molecule of the Week. Retrieved April 22, 2025

Ayyam, T. M., Sivasankari, S., & Sankaranarayanan, M. *(2025).* Nano-inspired optimized valorization of agrowastes by Vagococcus fluvialis. Cleaner Waste Systems, 6, 100096.

Baker, P. J., Turnbull, A., Sedelnikova, S. *E., Stillman, T.* J., Engel, P. C., & Rice, D. W. (1998). A role for quaternary structure in the substrate specificity of glutamate dehydrogenase. Structure, 6(7), 801–810.

Chen, W., Zhang, Y., Liu, Z., Wang, X., & Li, J. (2023). *Alanine dehydrogenases from four different microorganisms: Characterization and their application in L-alanine production*. Biotechnology for Biofuels and Bioproducts, 16, 23.

Dave, U. C., & Kadeppagari, R. *K*. (2019). Alanine dehydrogenase and its applications – A review. Critical Reviews in Biotechnology, 39(5), 648–664.

Drenth, J. (2007). *Principles of Protein X-ray Crystallography (3rd ed.)*. Springer.

Ertem, B., Yilmaz, M., & Demirci, H. (2022). *High-throughput microbatch under oil crystallization and X-ray structure determination at Turkish Light Source 'Turkish DeLight'*. bioRxiv.

Feller, G., & Gerday, C. (2003). *Psychrophilic enzymes: Hot topics in cold adaptation*. Nature Reviews Microbiology, 1(3), 200–208.

Galkin, A., Kulakova, L., Yamamoto, H., & Esaki, N. (1999). *Cold-adapted alanine dehydrogenases from two Antarctic bacterial strains: Gene cloning, protein characterization, and application to L-alanine production*. Journal of Bacteriology, 181(14), 4348–4353.

Garcia, V., Abat, C., & Rolain, J.-M. (2016). *Report of the first Vagococcus lutrae human infection, Marseille, France*. New Microbes and New Infections, 9, 56–57.

Gerharz, T., Reichl, U., & Gilles, E. D. *(2005).* Optimization of pyruvate production with Corynebacterium glutamicum under oxygen deprivation conditions. Biotechnology and Bioengineering, 92(1), 129–140.

Glusker, J. P., Lewis, M., & Rossi, M. *(1994).* Crystal Structure Analysis for Chemists and Biologists. VCH Publishers.

Gray, L. R., Tompkins, S. *C., & Taylor, E.* B. (2014). Regulation of pyruvate metabolism and human disease. Cellular and Molecular Life Sciences, 71(14), 2577–2604.

Hanukoglu, I. (2015). *Proteopedia: Rossmann fold: A ubiquitous motif in proteins*. Biochemistry and Molecular Biology Education, 43(3), 206–209.

Hols, P., Kleerebezem, M., Schanck, A. N., Ferain, T., Siezen, R. *J., & De Vos, W.* M. (1999). Conversion of Lactococcus lactis from homolactic to homoalanine fermentation through metabolic engineering. Applied and Environmental Microbiology, 65(12), 5001–5007.

Janin, J., Bahadur, R. P., & Chakrabarti, P. *(2008).* Protein–protein interaction and quaternary structure. Quarterly Reviews of Biophysics, 41(2), 133–180.

Jumper, J., Evans, R., Pritzel, A., et al. (2021). *Highly accurate protein structure prediction with AlphaFold.* Nature, 596, 583–589.

Kantardjieff, K. A., & Rupp, B. *(2003).* Matthews coefficient probabilities: Improved estimates for unit cell contents of proteins, DNA, and protein–nucleic acid complex crystals. Protein Science, 12(9), 1865–1871.

Knaus, T., Bastian, S., & Mutti, F. G. *(2016).* Kinetic resolution of racemic amines to enantiopure (S)-amines by a biocatalytic cascade employing amine dehydrogenase and alanine dehydrogenase. Green Chemistry, 18(3), 453–457.

Knaus, T., Böhmer, W., Mutti, F. G., & Turner, N. *J.* (2016). Biocatalytic amination–reduction cascades: Development and application. ChemCatChem, 8(1), 51–55.

Kobayashi, J., Furukawa, Y., Okabe, M., & Shimizu, H. (2014). *Overproduction of alanine by Arthrobacter strains with glucose-nonrepressible L-alanine dehydrogenase*. Journal of Bioscience and Bioengineering, 118(4), 430–436.

Krissinel, E., & Henrick, K. (2007). *Inference of macromolecular assemblies from crystalline state*. Journal of Molecular Biology, 372(3), 774–797.

Krissinel, E., & Henrick, K. (2007). *Inference of macromolecular assemblies from crystalline state*. Journal of Molecular Biology, 372(3), 774–797.

Laskowski, R. A., & Swindells, M. *B*. (2011). LigPlot+: Multiple ligand–protein interaction diagrams for drug discovery. Journal of Chemical Information and Modeling, 51(10), 2778–2786.

Lawson, P. A., Foster, G., Falsen, E., Ohlen, M., & Collins, M. *D*. (1999). Vagococcus lutrae sp. nov., isolated from the common otter (Lutra lutra). International Journal of Systematic Bacteriology, 49, 1251–1254.

Lengauer, T., & Rarey, M. (1996). *Computational methods for biomolecular docking*. Current Opinion in Structural Biology, 6(3), 402–406.

Lennarz, W. J., & Lane, M. *D*. (2021). Encyclopedia of Biological Chemistry (2nd ed.). Academic Press.

Lesk, A. M. *(1995).* NAD-binding domains of dehydrogenases. Current Opinion in Structural Biology, 5(6), 775–783.

Lesk, A. M. *(1995).* NAD-binding domains of dehydrogenases. Current Opinion in Structural Biology, 5(6), 775–783.

Letunic, I., & Bork, P. (2021). *Interactive Tree Of Life (iTOL) v5: an online tool for phylogenetic tree display and annotation*. Nucleic Acids Research, 49(W1), W293–W296.

Li, Y., Wang, C., He, J., & Wang, M. (2024). *Fusion of formate dehydrogenase and alanine dehydrogenase as an amino donor regeneration system*. JACS Au, 4(2), 335–344.

Liu, Y., Feng, Y., Xu, Z., Zhang, X., & Xu, L. (2022). *CB-Dock2: Improved protein–ligand blind docking by integrating cavity detection, docking, and homologous template fitting*. Nucleic Acids Research, 50(W1), W159–W164.

Luo, X., Ye, Y., Lin, Z., Chen, D., & Liu, X. (2022). *Electrochemical biosensor for L-phenylalanine based on phenylalanine dehydrogenase and conductive polymer nanostructure*. Bioelectrochemistry, 146, 108179.

Maeno, M., Gu, P., Ma, Q., Zhao, S., Li, Q., & Gao, J. (2023). *Alanine dehydrogenases from four different microorganisms: Characterization and their application in L-alanine production*. Biotechnology for Biofuels and Bioproducts, 16(1), 123.

Maia, L. B., Moura, J. *J*. G., & Moura, I. (2017). Molybdenum and tungsten-containing

formate dehydrogenases: An old enzyme enigma. Biochemical Society Transactions, 45(5), 1305–1313.

Matthews, B. W. *(1968).* Solvent content of protein crystals. Journal of Molecular Biology, 33(2), 491–497.

Morris, G. M., & Lim-Wilby, M. *(2008).* Molecular docking. In Molecular Modeling of Proteins (pp. 365–382). Humana Press.

Ohshima, T., & Soda, K. (1979). *Crystalline L-alanine dehydrogenase: Purification, crystallization, and properties*. The Journal of Biochemistry, 86(1), 111–120.

Ohshima, T., & Soda, K. (1990). *Biochemistry and biotechnology of amino acid dehydrogenases*. In A. Fiechter (Ed.), Advances in Biochemical Engineering/Biotechnology (Vol. 42, pp. 188–206). Springer-Verlag.

O'Connor, R. J., & Halvorson, H. *O*. (1961). L-alanine dehydrogenase: A mechanism controlling the specificity of amino acid-induced germination of Bacillus cereus spores. Journal of Bacteriology, 82(5), 706–713.

Padrosa, A., Klement, T., Frahm, B., & Krull, R. (2021). *Overexpression of genes encoding glycolytic enzymes in Corynebacterium glutamicum enhances glucose metabolism and alanine production under oxygen deprivation conditions*. Biotechnology and Bioengineering, 118(10), 3870–3882.

Pietruszko, R., Sexton, H. B., & Vennesland, B. *(1965).* The substrate specificity of alanine dehydrogenase. Archives of Biochemistry and Biophysics, 112(3), 573–579.

Salgado, A. C., Pérsico, A. *C., & de Sá Almeida, M*. A. (2023). Identification of a novel two-peptide lantibiotic from Vagococcus fluvialis. Microbiology Spectrum, 11(5), e00954-22.

Schrödinger, LLC. (2015). *The PyMOL Molecular Graphics System, Version 1.8.*

Sievers, F., & Higgins, D. G. *(2014).* Clustal Omega, accurate alignment of very large numbers of sequences. Methods in Molecular Biology, 1079, 105–116.

Siranosian, K. J., Grossman, A. *D., & Losick, R*. (1993). Alanine dehydrogenase (ald) is required for normal sporulation in Bacillus subtilis. Journal of Bacteriology, 175(6), 1772–1779.

UniProt Consortium. (2024). *Uridylate kinase (pyrH) – Vagococcus salmoninarum (strain ATCC 49156) [UniProt protein entry A0A429ZEQ1].* Retrieved May 6, 2025.

Vadas, T. M., & Whitehead, T. *A*. (2008). Room-temperature synthesis of L-alanine using the alanine dehydrogenase of the thermophile Thermus thermophilus. Biotechnology Progress, 24(4), 839–843.

Wakayama, M., Kanda, K., Ohshima, T., & Soda, K. (1998). *Structural studies of NAD+-dependent L-alanine dehydrogenase from Phormidium lapideum*. Journal of Biochemistry, 123(6), 1141–1149.

Wakayama, M., Shimizu, H., & Okabe, M. (2008). *Room-temperature synthesis of L-alanine using the alanine dehydrogenase of the thermophile Thermus thermophilus*. Biotechnology Progress, 24(4), 839–843.

Wang, Q., Jiang, Y., Hu, Y., Wang, J., Wang, X., & Yu, H. (2023). *Metabolic engineering of Escherichia coli for the production of -ketovalerate as a biofuel precursor*. ACS Synthetic Biology, 12(1), 143–153.

Xu, Y., Chu, H., Huang, Q., & Su, Z. (2008). *Pyruvate production by Torulopsis glabrata: Fermentation optimization and repeated batch culture*. Journal of Industrial Microbiology & Biotechnology, 35(12), 1437–1442.

Yang, J., Roy, A., & Zhang, Y. (2013). *Protein–ligand binding site recognition using complementary binding-specific substructure comparison and sequence profile alignment*. Bioinformatics, 29(20), 2588–2595.

Yuan, W., Du, Y., Yu, K., Xu, S., Liu, M., Wang, S., ... & Sun, J. *(2022)*. The production of pyruvate in biological technology: A critical review. Microorganisms, 10(12), 2454.

Zangari, J., Petrelli, F., Maillot, B., & Martinou, J. C. *(2020)*. The multifaceted pyruvate metabolism: Role of the mitochondrial pyruvate carrier. Biomolecules, 10(7), 1068.

Zhang, C., Liu, Y., & Yang, J. (2005). *CB-Dock: A web server for cavity detection-guided protein–ligand blind docking*. Bioinformatics, 21(5), 605–611.

Zhou, Y., Lin, H., & Liang, F. (2023). *Engineering alanine dehydrogenase to favor a non-natural cofactor nicotinamide cytosine dinucleotide*. ACS Synthetic Biology, 12(7), 1892–1901.

Zhou, Z., Li, X., Ren, J., Wu, H., & Zhang, Y. (2022). *Characterization of a leucine dehydrogenase from Pseudomonas balearica and its application in chiral amine synthesis*. Catalysts, 12(9), 971.

Zhou, Z., Ren, J., Chen, X., & Zhang, Y. (2023). *Engineering of leucine dehydrogenase*

for improved activity towards bulky substrates via semi-rational design. Journal of Molecular Catalysis B: Enzymatic, 194, 106854.

Ågren, D., Stehr, M., Berthold, C. L., Kapoor, S., Oehlmann, W., Singh, M., & Schneider, G. *(2008)*. Three-dimensional structures of apo- and holo-L-alanine dehydrogenase from Mycobacterium tuberculosis reveal conformational changes upon coenzyme binding. Journal of Molecular Biology, 377(4), 1161–1173.

Appendix A

CHEMICALS

Kanamycin	GOLDBIO
Glycerol	ISOLAB
Imidazole	BioFroxx
IPTG	GOLDBIO
LB Agar	Caisson
NaCl	ISOLAB
HCl	ISOLAB
Ni-NTA	QIAGEN
Paraffin Oil	Tekkim Kimya
SDS	Sigma-Aldrich
Tris Base	Sigma-Aldrich
Triton X-100	Sigma-Aldrich
Tryptone	BD Biosciences
Yeast Extract	BD Biosciences

Appendix B

EQUIPMENT

ÅKTA go	Cytiva
Beckman Allegra 15R Centrifuge	Beckman Coulter
Beckman Avanti J-26S	Beckman Coulter
Beckman Optima™ L-80 XP Ultracentrifuge	Beckman Coulter
Beckman Ti-45 Rotor	Beckman Coulter
Branson W250 Sonifier	Branson
Cryovials	Wuxi NEST Biotechnology
Falcon Tubes	FIRATMED
Innova 44R	Eppendorf
Innova 4430R	New Brunswick
Kimtech Science KimWipes	Kimberly-Clark
NanoDrop™ 2000c	Thermo Scientific
Terasaki Plates	Greiner Bio-One
TGX-Mini Protean Gradient SDS-PAGE System	Bio-Rad Laboratories
Millipore Milli-Q Water Purification System	Merck Millipore
Oxford Cryosystems Cryostream 800 Plus	Oxford Cryosystems
Rigaku XtaLAB Synergy Flow XRD	Rigaku

Appendix C

PROTEIN LADDER

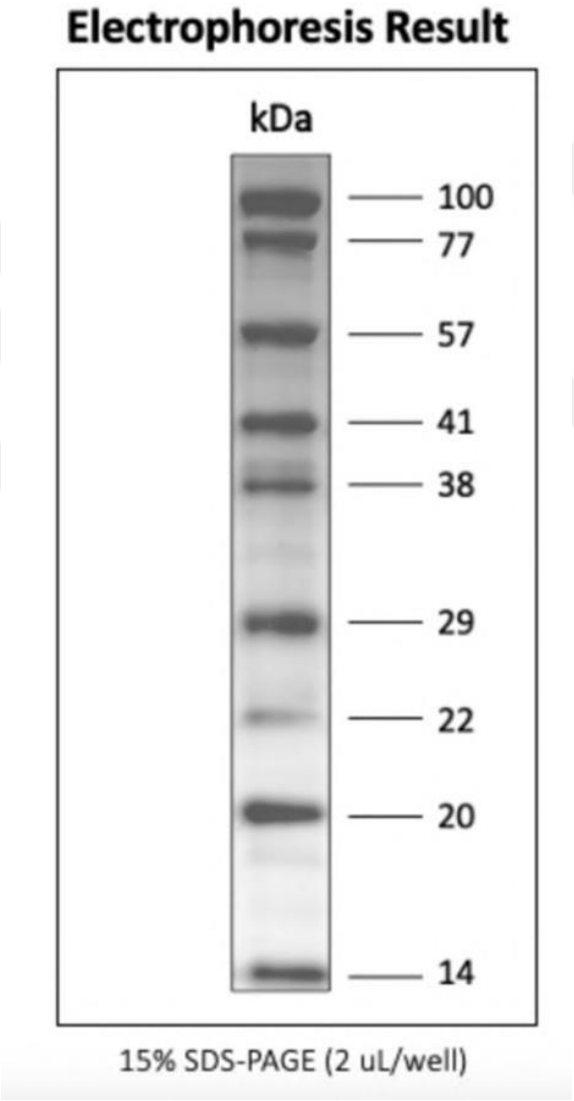

Figure C.1: KUYBIIG-M Protein Ladder

Appendix D

CRYSTALLIZATION SCREENING SOLUTIONS

3D Structure Screen	Molecular Dimensions
Clear Strategy Screen	Molecular Dimensions
Crystal Screen	Hampton Research
Crystal Screen Cryo	Hampton Research
Grid Screen Ammonium Sulfate	Hampton Research
Grid Screen MPD	Hampton Research
Grid Screen PEG/LiCl	Hampton Research
Grid Screen PEG6000	Hampton Research
Grid Screen Sodium Chloride	Hampton Research
Helix	Molecular Dimensions
Index	Hampton Research
Ionic Liquid Screen	Hampton Research
JBSscreen Nuc-Pro	Jena Bioscience
JCSG	Molecular Dimensions
MacroSol	Molecular Dimensions

MembFac	Hampton Research
MIDAS	Molecular Dimensions
Morpheus	Molecular Dimensions
MultiXtal	Molecular Dimensions
Natrix	Hampton Research
NeXtal Protein Complex Suite	NeXtal Biotechnologies
NR-LBD	Molecular Dimensions
PACT Premier	Molecular Dimensions
PEG/Ion	Hampton Research
PEGRx	Hampton Research
PGA Screen	Molecular Dimensions
ProPlex Screen	Molecular Dimensions
Quik Screen	Hampton Research
SaltRx	Hampton Research
Structure Screen	Molecular Dimensions
Stura FootPrint Screen	Molecular Dimensions
Wizard	Rigaku
Wizard Cryo	Rigaku
Wizard Precipitant Synergy	Rigaku